13 Neutrinos and neutrino oscillations

This chapter focusses on the properties of neutrinos and in particular the phenomenon of neutrino oscillations, whereby neutrinos undergo flavour transitions as they propagate over large distances. Neutrino oscillations are a quantum-mechanical phenomenon and can be described in terms of the relationship between the eigenstates of the weak interaction ν_e, ν_μ and ν_τ, and the eigenstates of the free-particle Hamiltonian, known as the mass eigenstates, ν_1, ν_2 and ν_3. The mathematical description of neutrino oscillations is first introduced for two flavours and then extended to three flavours. The predictions are compared to the recent experimental data from reactor and long-baseline neutrino oscillation experiments.

13.1 Neutrino flavours

Unlike the charged leptons, which can be detected from the continuous track defined by the ionisation of atoms as they traverse matter, neutrinos are never directly observed; they are only detected through their weak interactions. Different neutrino flavours can only be distinguished by the flavours of charged lepton produced in charged-current weak interactions. Consequently, the electron neutrino ν_e, is *defined* as the neutrino state produced in a charged-current weak interaction along with an electron. Similarly, by definition, the weak charged-current interactions of a ν_e will produce an electron. For many years it was assumed that the ν_e, ν_μ and ν_τ were massless fundamental particles. This assumption was based, at least in part, on experimental evidence. For example, it was observed that the interactions of the neutrino/antineutrino produced along with a positron/electron in a nuclear β-decay, would produce an electron/positron as indicated in Figure 13.1. This naturally led to the idea that the electron neutrino carried some property related to the electron that is conserved in weak interactions, which was referred to as electron number. Similarly, in beam neutrino experiments, such as those described in Chapter 12, it was observed that the neutrinos produced from $\pi^+ \to \mu^+\nu_\mu$ decays always produced a muon in charged-current weak interactions.

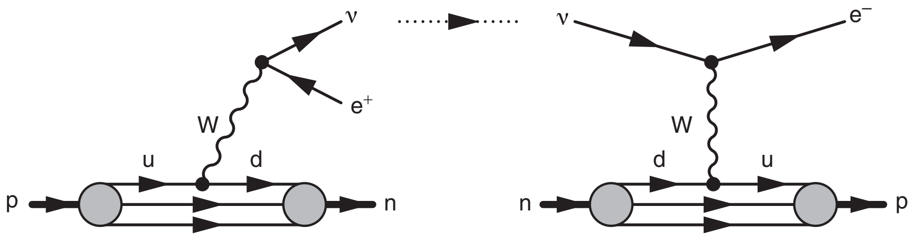

Fig. 13.1 Neutrino production and subsequent detection where the ν_e state is associated with positrons/electrons.

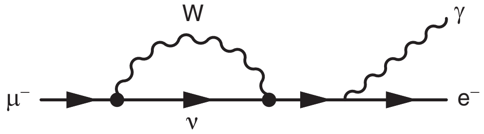

Fig. 13.2 A possible Feynman diagram for $\mu^- \to e^-\gamma$ for the case where the ν_e and ν_μ are not distinct.

Further evidence for the distinct nature of the electron and muon neutrinos was provided by the non-observation of the decay $\mu^- \to e^-\gamma$, which is known to have a very small branching ratio,

$$BR(\mu^- \to e^-\gamma) < 10^{-11}.$$

In principle, this decay could occur via the Feynman diagram shown in Figure 13.2. The absence of the decay suggests that the neutrino associated with $W\mu^-\nu$ vertex is distinct from the neutrino associated with the $We^-\nu$ vertex.

Until the late 1990s, relatively little was known about neutrinos beyond that there are three distinct flavours and that they are extremely light (and possibly massless). However, even at that time several experiments had reported possible anomalies in the observed interaction rates of atmospheric and solar neutrinos. This picture changed with the publication of the solar and atmospheric neutrino data from the Super-Kamiokande detector, which provided compelling experimental evidence for the phenomenon of neutrino flavour oscillations over very large distances. The subsequent study of neutrino oscillations has been one of the highlights of particle physics in recent years.

13.2 Solar neutrinos

Nuclear fusion in the Sun produces a large flux of electron neutrinos, $2\times10^{38}\,\nu_e\,\mathrm{s}^{-1}$. Despite the smallness of neutrino interaction cross sections and the large distance to the Sun, solar neutrinos can be observed with a sufficiently massive detector. Nuclear fusion in the Sun proceeds through a number of distinct processes, each of which has several stages. The resulting solar neutrino energy spectrum is shown in

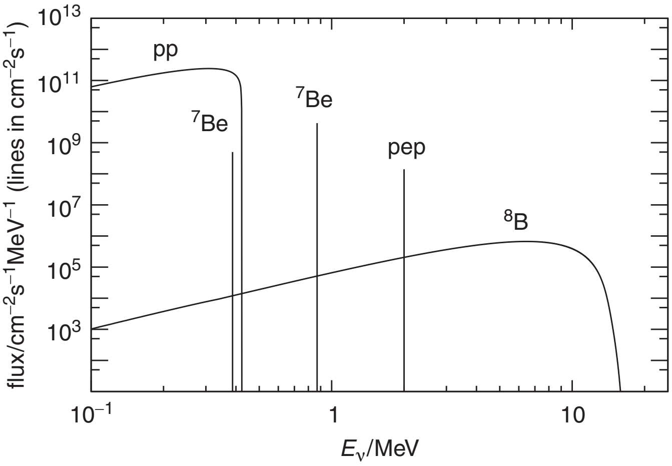

Fig. 13.3 The flux of solar neutrinos from the main processes in the Sun. The two ^{7}Be lines are from the electron capture reactions $^7\mathrm{Be} + \mathrm{e}^- \to {}^7\mathrm{Li} + \nu_\mathrm{e}$. The pep line is from $\mathrm{p} + \mathrm{e}^- + \mathrm{p} \to {}^2\mathrm{H} + \nu_\mathrm{e}$. Adapted from Bahcall and Pinsonneault (2004).

Figure 13.3. The main hydrogen burning process, known as the pp cycle, proceeds through three steps:

$$\begin{aligned} \mathrm{p} + \mathrm{p} &\to \mathrm{D} + \mathrm{e}^+ + \nu_\mathrm{e}, \\ \mathrm{D} + \mathrm{p} &\to {}^3_2\mathrm{He} + \gamma, \\ {}^3_2\mathrm{He} + {}^3_2\mathrm{He} &\to {}^4_2\mathrm{He} + \mathrm{p} + \mathrm{p}. \end{aligned}$$

Because the binding energy of the deuteron $^2_1\mathrm{D}$ is only 2.2 MeV, the neutrinos produced in the process $\mathrm{p}+\mathrm{p} \to \mathrm{D}+\mathrm{e}^+ +\nu_\mathrm{e}$ have low energies, $E_\nu < 0.5$ MeV. Consequently, they are difficult to detect. For this reason, the majority of experiments have focussed on the detection of the higher-energy solar neutrinos from rarer fusion processes. The highest energy solar neutrinos originate from the β-decay of boron-8 (^{8}B) that is produced from the fusion of two helium nuclei,

$$\begin{aligned} {}^4_2\mathrm{He} + {}^3_2\mathrm{He} &\to {}^7_4\mathrm{Be} + \gamma, \\ {}^7_4\mathrm{Be} + \mathrm{p} &\to {}^8_5\mathrm{B} + \gamma, \end{aligned}$$

with the subsequent β-decay,

$${}^8_5\mathrm{B} \to {}^8_4\,\mathrm{Be}^* + \mathrm{e}^+ + \nu_\mathrm{e},$$

giving neutrinos with energies up to 15 MeV.

A number of experimental techniques have been used to detect solar neutrinos. The earliest experiment, based in the Homestake Mine in South Dakota, USA, used a radiochemical technique to measure the flux of solar neutrinos. It consisted of a tank of 615 tons of dry-cleaning fluid, C_2Cl_4. The solar neutrino flux was measured by counting the number of ^{37}Ar atoms produced in the inverse β-decay process, $\nu_e + {}^{37}_{17}\mathrm{Cl} \to {}^{37}_{18}\mathrm{Ar} + e^-$. The ^{37}Ar atoms where extracted from the tank and counted through their radioactive decays. Despite the huge flux of neutrinos, only 1.7 interactions per day were expected. The observed rate was only 0.48 ± 0.04 neutrino interactions per day; see Cleveland *et al.* (1998). This apparent deficit of solar neutrinos became known as the solar neutrino problem. The Homestake experiment was sensitive to the relatively high-energy ^{8}B neutrinos. Subsequently, the SAGE and GALLEX radiochemical experiments used gallium as a target, and were sensitive to the low-energy neutrinos from the first step of the pp chain. These experiments also observed a deficit of solar neutrinos.

Radiochemical experiments played an important role in demonstrating the existence of the solar neutrino deficit; Ray Davis, who conceived the Homestake experiment, was awarded the Nobel prize for its discovery. However, it was the results from the large water Čerenkov detectors that firmly established the origin of the deficit of solar neutrinos.

13.2.1 The Super-Kamiokande experiment

The 50 000 ton Super-Kamiokande water Čerenkov detector, shown schematically in Figure 13.4a, was designed to detect Čerenkov radiation (see Section 1.2.1) from relativistic particles produced within the volume of the detector. In essence, Super-Kamiokande is a large vessel of water surrounded by photo-multiplier tubes (PMTs) that are capable of detecting single photons.

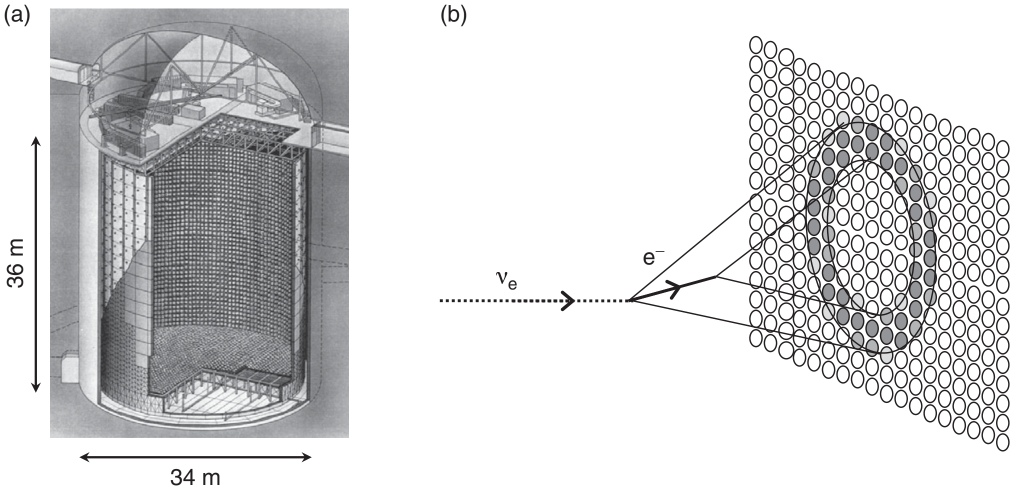

Fig. 13.4 (a) The Super-Kamiokande experiment comprising a tank of 50 000 tons of water viewed by 11 146 PMTs. (b) A neutrino interaction in the Super-Kamiokande experiment showing the ring of Čerenkov light produced by the relativistic e^- with $v > c/n$ as detected as signals in the PMTs on the walls of the detector. Left-hand diagram courtesy of the Super-Kamiokande collaboration.

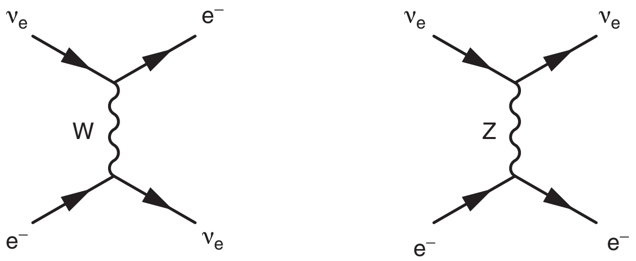

Fig. 13.5 The two Feynman diagrams contributing to $\nu_e e^- \to \nu_e e^-$ elastic scattering.

Because oxygen is a particularly stable nucleus, the charged-current process $\nu_e + {}^{16}_{8}\mathrm{O} \to {}^{16}_{9}\mathrm{F} + e^-$ is kinematically forbidden for the neutrino energies being considered here. Consequently, solar neutrinos are detected by the elastic scattering process $\nu_e e^- \to \nu_e e^-$, shown in Figure 13.5. The final-state electron is relativistic and can be detected from the Čerenkov radiation photons that are emitted at a fixed angle to its direction of motion as it travels through water. The photons form a ring of hits in the PMTs on the sides of the detector, as shown in Figure 13.4b. The number of detected photons provides a measure of the neutrino energy and the direction of the electron can be determined from the orientation of the Čerenkov ring. In this way, Super-Kamiokande is able to detect electron neutrino elastic scattering interactions down to neutrino energies of about 5 MeV. Below this energy, background from the β-decays of radioisotopes dominates. Because of this effective threshold, the Super-Kamiokande detector is sensitive primarily to the flux of ^{8}B neutrinos.

The angular distribution of the scattered electron with respect to the incoming neutrino direction is isotropic in the centre-of-mass frame, as was the case for neutrino–quark scattering cross section of (12.13). Because the centre-of-mass frame is boosted in the direction of the neutrino, in the laboratory frame the scattered electron tends to follow the direction of the solar neutrino. Consequently, the directional correlation with the Sun is retained.

Figure 13.6 shows the reconstructed electron direction with respect to the direction of the Sun for neutrino interactions with $E_\nu \gtrsim 5\,\mathrm{MeV}$. The peak towards $\cos\theta_{\mathrm{sun}} = 1$ provides clear evidence for a flux of neutrinos from the Sun. The flat background arises from the β-decay of radioisotopes. Whilst Super-Kamiokande observes clear evidence of solar neutrinos from the Sun, the flux of electron neutrinos is measured to be about half that expected.

13.2.2 The SNO experiment

Results from Super-Kamiokande and other solar neutrino experiments demonstrated a clear deficit of electron neutrinos from the Sun. The Sudbury Neutrino Observatory (SNO) experiment in Canada was designed to measure both the ν_e and *total*

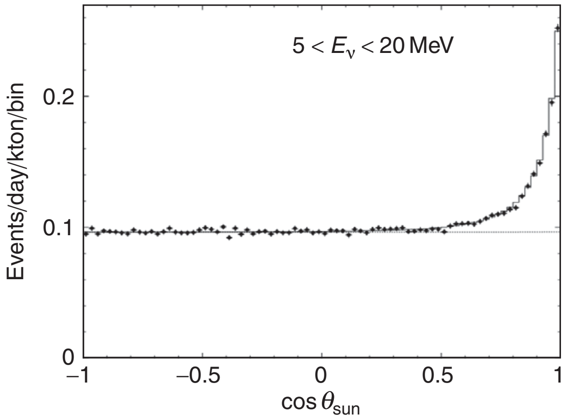

Fig. 13.6 The Super-Kamiokande solar neutrino data plotted as a function of the cosine of the polar angle of the electron with respect to the direction of the Sun. From Fukada *et al.* (2001).

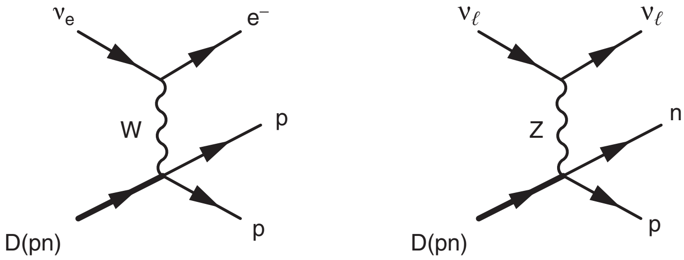

Fig. 13.7 The ν_e charged-current (CC) and neutral-current (NC) weak interactions with the deuteron.

neutrino flux from the Sun. SNO consisted of 1000 tons of heavy water, D_2O, inside a 12 m diameter vessel, viewed by 9,600 PMTs. Heavy water was used because the deuteron, the bound state of a proton and a neutron, has a binding energy of just 2.2 MeV, which is relatively small compared to the energies of the ^{8}B solar neutrinos. For this reason, solar neutrinos can be detected in SNO through three different physical processes. Crucially, the different processes have different sensitivities to the fluxes of electron, muon and tau neutrinos, $\phi(\nu_e)$, $\phi(\nu_\mu)$ and $\phi(\nu_\tau)$.

Because of the low binding energy of the deuteron, the charged-current (CC) interaction of electron neutrinos, $\nu_e + D \rightarrow e + p + p$, shown in Figure 13.7 (left), is kinematically allowed. The final-state electron can be detected from the resulting Čerenkov ring. From the discussion of Section 12.2.2, it can be appreciated that in the centre-of-mass frame the angular distribution of the electron relative to the incoming neutrino is almost isotropic. Because $E_\nu \ll m_D$, the laboratory frame is almost equivalent to the centre-of-mass frame and therefore the final-state electron does not correlate strongly with the direction of the Sun. The charged-current interaction with the deuteron is only sensitive to the ν_e flux and therefore

$$\text{CC rate} \propto \phi(\nu_e). \tag{13.1}$$

All flavours of neutrinos can interact with the deuteron via the neutral-current (NC) interaction of Figure 13.7 (right), where the momentum imparted to the deuteron is sufficient to break up this loosely bound state. The neutron produced in the final state will (eventually) be captured in the reaction $\mathrm{n} + {}^{2}_{1}\mathrm{H} \rightarrow {}^{3}_{1}\mathrm{H} + \gamma$, releasing a 6.25 MeV photon. Through its subsequent interactions, this photon will produce relativistic electrons that give a detectable Čerenkov signal. The neutral-current process is equally sensitive to all neutrino flavours, thus

$$\text{NC rate} \propto \phi(\nu_e) + \phi(\nu_\mu) + \phi(\nu_\tau). \tag{13.2}$$

Finally, neutrinos can interact with the atomic electrons through the elastic scattering (ES) processes of Figure 13.5. For electron neutrinos, both the charged-current process and the neutral-current process contribute to the cross section, whereas for ν_μ and ν_τ only the neutral-current process, which has a smaller cross section, contributes. The observed elastic scattering rate is therefore sensitive to all flavours of neutrinos but has greater sensitivity to ν_e,

$$\text{ES rate} \propto \phi(\nu_e) + 0.154\left[\phi(\nu_\mu) + \phi(\nu_\tau)\right]. \tag{13.3}$$

The electrons from the ES scattering process point back to the Sun and can therefore be distinguished from those from the CC process.

The different angular and energy distributions of the Čerenkov rings from CC, NC and ES interactions allows the rates for each individual process to be determined separately. Using the knowledge of the interaction cross sections, the measured rates can be interpreted in terms of the neutrino fluxes using (13.1)–(13.3), with the CC process providing a measure of the ν_e flux and the NC process providing a measure of the total neutrino flux ($\nu_e + \nu_\mu + \nu_\tau$). The observed CC rate was consistent with a flux of ν_e of $1.8 \times 10^{-6}\,\mathrm{cm}^{-2}\,\mathrm{s}^{-1}$ and the observed NC rate was consistent with a total neutrino flux of $5.1 \times 10^{-6}\,\mathrm{cm}^{-2}\,\mathrm{s}^{-1}$, providing clear evidence for an unexpected ν_μ/ν_τ flux from the Sun.

The observed neutrino rates in SNO from the CC, NC and ES processes can be combined to place constraints on the separate ν_e and $\nu_\mu + \nu_\tau$ fluxes, as shown in Figure 13.8, giving the overall result

$$\phi(\nu_e) = (1.76 \pm 0.10) \times 10^{-6}\,\mathrm{cm}^{-2}\,\mathrm{s}^{-1},$$
$$\phi(\nu_\mu) + \phi(\nu_\tau) = (3.41 \pm 0.63) \times 10^{-6}\,\mathrm{cm}^{-2}\,\mathrm{s}^{-1}.$$

The total neutrino flux, obtained from the NC process is consistent with the expectation from theoretical modelling of the Sun that predicts a ν_e flux of

$$\phi(\nu_e)_{pred} = (5.1 \pm 0.9) \times 10^{-6}\,\mathrm{cm}^{-2}\,\mathrm{s}^{-1}.$$

The SNO data therefore demonstrate that the total flux of neutrinos from the Sun is consistent with the theoretical expectation, but rather than consisting of only ν_e, there is a large ν_μ and/or ν_τ component. Since ν_μ/ν_τ cannot be produced in

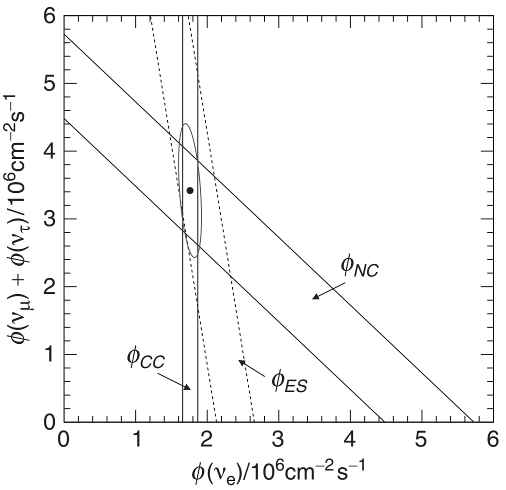

Fig. 13.8 The constraints on the ν_e and $\nu_\mu+\nu_\tau$ fluxes from the Sun from SNO data. The bands indicate the one standard deviation errors from the different processes. The CC process is sensitive only to ν_e. The NC process is sensitive to all neutrinos. The ES rate is proportional to $\phi(\nu_e) + 0.154\left[\phi(\nu_\mu) + \phi(\nu_\tau)\right]$. The ellipse is the resulting 68% confidence limit from combining the three measurements. Adapted from Ahmad *et al.* (2002).

the fusion processes in the Sun, SNO provides clear evidence of neutrino flavour transformations over large distances.

13.3 Mass and weak eigenstates

The neutrino flavour transformations observed by SNO and other experiments can be explained by the phenomenon of neutrino oscillations. The physical states of particle physics, termed the mass eigenstates, are the stationary states of the free-particle Hamiltonian and satisfy

$$\hat{H}\psi = i\frac{\partial\psi}{\partial t} = E\psi.$$

The time evolution of a mass eigenstate takes the form of (2.25),

$$\psi(\mathbf{x},t) = \phi(\mathbf{x})e^{-iEt}.$$

The neutrino mass eigenstates (the fundamental particles) are labelled ν_1, ν_2 and ν_3. There is no reason to believe that the mass eigenstates should correspond to the weak eigenstates, ν_e, ν_μ and ν_τ, which are produced along with the respective flavour of charged lepton in a weak interaction. This important distinction between mass and weak eigenstates is illustrated in Figure 13.9. Here any one of the three mass eigenstates can be produced in conjunction with the electron in the initial

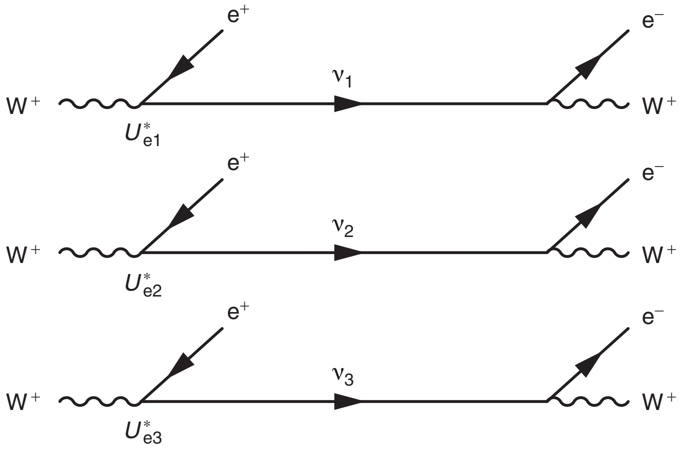

Fig. 13.9 The $We^+\nu_e$ vertex in terms of the mass eigenstates.

weak interaction. Since it is not possible to know which mass eigenstate was produced, the system has to be described by a coherent linear superposition of ν_1, ν_2 and ν_3 states. In quantum mechanics, the basis of weak eigenstates can be related to the basis of mass eigenstates by a unitary matrix U,

$$\begin{pmatrix} \nu_e \\ \nu_\mu \\ \nu_\tau \end{pmatrix} = \begin{pmatrix} U_{e1} & U_{e2} & U_{e3} \\ U_{\mu 1} & U_{\mu 2} & U_{\mu 3} \\ U_{\tau 1} & U_{\tau 2} & U_{\tau 3} \end{pmatrix} \begin{pmatrix} \nu_1 \\ \nu_2 \\ \nu_3 \end{pmatrix}. \tag{13.4}$$

Hence the electron neutrino, which is the quantum state produced along with a positron in a charged-current weak interaction, is the linear combination of the mass eigenstates defined by the relative charged-current weak interaction couplings of the ν_1, ν_2 and ν_3 at the $W^+ \to e^+\nu$ vertex

$$|\psi\rangle = U^*_{e1}|\nu_1\rangle + U^*_{e2}|\nu_2\rangle + U^*_{e3}|\nu_3\rangle. \tag{13.5}$$

The neutrino state subsequently propagates as a coherent linear superposition of the three mass eigenstates until it interacts and the wavefunction collapses into a weak eigenstate, producing an observable charged lepton of a particular flavour. If the masses of the ν_1, ν_2 and ν_3 are not the same, phase differences arise between the different components of the wavefunction and the phenomenon of neutrino oscillations occurs. In this way, a neutrino produced along with one flavour of charged lepton can interact to produce a charged lepton of a different flavour.

13.3.1 The leptonic charged-current vertex revisited

In Chapter 12, the charged-current interaction between a charged lepton and a neutrino was described in terms of the neutrino weak eigenstates. For example, the weak charged-current vertex has the form

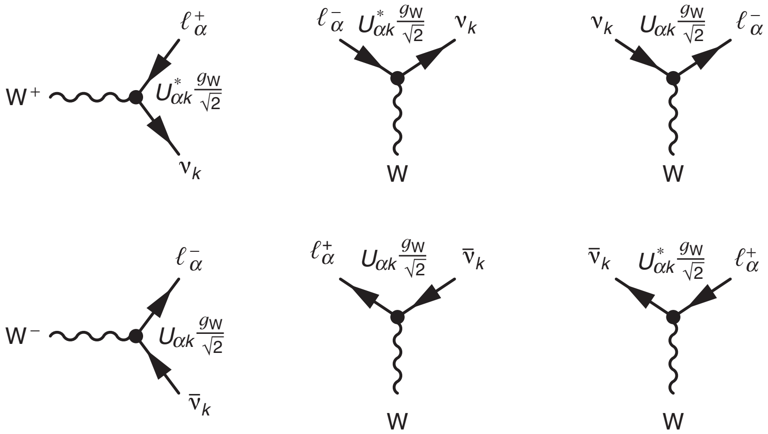

Fig. 13.10 The charged-current weak interaction vertices for charged lepton of flavour $\alpha = \mathrm{e}, \mu, \tau$ and a neutrino of type $k = 1, 2, 3$.

$$-i\frac{g_W}{\sqrt{2}}\bar{\mathrm{e}}\gamma^\mu\frac{1}{2}(1-\gamma^5)\nu_\mathrm{e},$$

where here ν_e and $\bar{\mathrm{e}}$ denote the electron neutrino spinor and the electron adjoint spinor. In terms of the neutrino mass eigenstates, the weak charged-current for a lepton of flavour $\alpha = \mathrm{e}, \mu, \tau$ and a neutrino of type $k = 1, 2, 3$ takes the form

$$\boxed{-i\frac{g_W}{\sqrt{2}}\bar{\ell}_\alpha\gamma^\mu\frac{1}{2}(1-\gamma^5)U_{\alpha k}\nu_k.}$$

Defining the neutrino state produced in a weak interaction using the matrix U of (13.4) implies that, when the neutrino appears as the adjoint spinor, the factor $U^*_{\alpha k}$ appears in the weak interaction vertex. Consequently, the couplings between neutrinos or antineutrinos and the charged leptons are those shown in Figure 13.10.

13.4 Neutrino oscillations of two flavours

The full treatment of neutrino oscillations for three flavours is developed in Section 13.5. However, the main features can be readily understood by considering just two flavours. For example, consider the weak eigenstates ν_e and ν_μ, which here are taken to be coherent linear superpositions of the mass eigenstates ν_1 and ν_2. The mass eigenstates propagate as plane waves of the form

$$|\nu_1(t)\rangle = |\nu_1\rangle e^{i(\mathbf{p}_1\cdot\mathbf{x}-E_1t)} = e^{-ip_1\cdot x},$$
$$|\nu_2(t)\rangle = |\nu_2\rangle e^{i(\mathbf{p}_2\cdot\mathbf{x}-E_2t)} = e^{-ip_2\cdot x},$$

where $(E_1, \mathbf{p}_1)$ and $(E_2, \mathbf{p}_2)$ are the respective energy and three-momenta of the ν_1 and ν_2, and $p\cdot x = Et - \mathbf{p}\cdot\mathbf{x}$ is the (Lorentz-invariant) phase. In the two-flavour

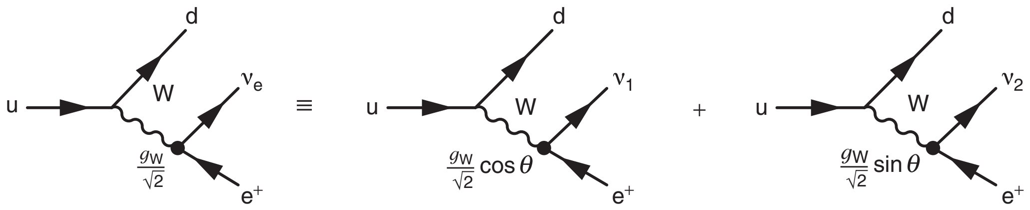

Fig. 13.11 Nuclear β-decay and its relation to the mass eigenstates for two flavours.

treatment of neutrino oscillations, the weak eigenstates are related to the mass eigenstates by a 2 × 2 unitary matrix that can be expressed in terms of a single mixing angle θ,

$$\begin{pmatrix} \nu_e \\ \nu_\mu \end{pmatrix} = \begin{pmatrix} \cos\theta & \sin\theta \\ -\sin\theta & \cos\theta \end{pmatrix} \begin{pmatrix} \nu_1 \\ \nu_2 \end{pmatrix}. \tag{13.6}$$

Now suppose at time $t = 0$, a neutrino is produced in the process $u \to de^+\nu_e$, as shown in Figure 13.11. The wavefunction at time $t = 0$ is the coherent linear superposition of ν_1 and ν_2, corresponding to the ν_e state

$$|\psi(0)\rangle = |\nu_e\rangle \equiv \cos\theta\,|\nu_1\rangle + \sin\theta\,|\nu_2\rangle.$$

The state subsequently evolves according to the time dependence of the mass eigenstates

$$|\psi(\mathbf{x}, t)\rangle = \cos\theta\,|\nu_1\rangle e^{-ip_1\cdot x} + \sin\theta\,|\nu_2\rangle e^{-ip_2\cdot x},$$

where p_1 and p_2 are the four-momenta associated with the mass eigenstates ν_1 and ν_2. If the neutrino then interacts at a time T and at a distance L along its direction of flight, the neutrino state at this space-time point is

$$|\psi(L, T)\rangle = \cos\theta\,|\nu_1\rangle e^{-i\phi_1} + \sin\theta\,|\nu_2\rangle e^{-i\phi_2}, \tag{13.7}$$

where the phases of the two mass eigenstates are written as

$$\phi_i = p_i\cdot x = E_i T - \mathrm{p}_i L.$$

Equation (13.7) can be written in terms of the weak eigenstates using the inverse of (13.6),

$$\begin{pmatrix} \nu_1 \\ \nu_2 \end{pmatrix} = \begin{pmatrix} \cos\theta & -\sin\theta \\ \sin\theta & \cos\theta \end{pmatrix} \begin{pmatrix} \nu_e \\ \nu_\mu \end{pmatrix},$$

leading to

$$\begin{aligned} |\psi(L, T)\rangle &= \cos\theta\left(\cos\theta\,|\nu_e\rangle - \sin\theta\,|\nu_\mu\rangle\right)e^{-i\phi_1} + \sin\theta\left(\sin\theta\,|\nu_e\rangle + \cos\theta\,|\nu_\mu\rangle\right)e^{-i\phi_2} \\ &= (e^{-i\phi_1}\cos^2\theta + e^{-i\phi_2}\sin^2\theta)\,|\nu_e\rangle - (e^{-i\phi_1} - e^{-i\phi_2})\cos\theta\sin\theta\,|\nu_\mu\rangle \\ &= e^{-i\phi_1}\left[(\cos^2\theta + e^{i\Delta\phi_{12}}\sin^2\theta)\,|\nu_e\rangle - (1 - e^{i\Delta\phi_{12}})\cos\theta\sin\theta\,|\nu_\mu\rangle\right], \end{aligned} \tag{13.8}$$

with

$$\Delta\phi_{12} = \phi_1 - \phi_2 = (E_1 - E_2)T - (\mathrm{p}_1 - \mathrm{p}_2)L. \tag{13.9}$$

If the phase difference $\Delta\phi_{12} = 0$, the neutrino remains in a pure electron neutrino state and will produce an electron in a subsequent weak charged-current interaction. However, if $\Delta\phi_{12} \neq 0$, there is now a muon neutrino component to the wavefunction. The relative sizes of the electron and muon neutrino components of the wavefunction can be obtained by writing (13.8) as

$$|\psi(L,T)\rangle = c_\mathrm{e}|\nu_\mathrm{e}\rangle + c_\mu|\nu_\mu\rangle,$$

where $c_\mathrm{e} = \langle\nu_\mathrm{e}|\psi\rangle$ and $c_\mu = \langle\nu_\mu|\psi\rangle$. The probability that the neutrino, which was produced as a ν_e, will interact to produce a muon is $P(\nu_\mathrm{e} \to \nu_\mu) = c_\mu c_\mu^*$. Comparison with (13.8) gives

$$\begin{aligned} P(\nu_\mathrm{e} \to \nu_\mu) = c_\mu c_\mu^* &= (1 - e^{i\Delta\phi_{12}})(1 - e^{-i\Delta\phi_{12}})\cos^2\theta\sin^2\theta \\ &= \tfrac{1}{4}(2 - 2\cos\Delta\phi_{12})\sin^2(2\theta) \\ &= \sin^2(2\theta)\sin^2\left(\frac{\Delta\phi_{12}}{2}\right). \end{aligned} \tag{13.10}$$

Hence, the $\nu_\mathrm{e} \to \nu_\mu$ oscillation probability depends on the mixing angle θ and the phase difference between the mass eigenstates, $\Delta\phi_{12}$. The derivation of the phase difference, $\Delta\phi_{12} = (E_1 - E_2)T - (\mathrm{p}_1 - \mathrm{p}_2)L$, in terms of the masses of ν_1 and ν_2 requires care. One could assume, without any real justification, that the momenta of the two mass eigenstates are equal, $\mathrm{p}_1 = \mathrm{p}_2 = \mathrm{p}$, in which case

$$\Delta\phi_{12} = (E_1 - E_2)T = \left[\mathrm{p}\left(1 + \frac{m_1^2}{\mathrm{p}^2}\right)^{\frac{1}{2}} - \mathrm{p}\left(1 + \frac{m_2^2}{\mathrm{p}^2}\right)^{\frac{1}{2}}\right]T. \tag{13.11}$$

Because $m \ll E$, the square roots in (13.11) are approximately,

$$\left(1 + \frac{m^2}{\mathrm{p}^2}\right)^{\frac{1}{2}} \approx 1 + \frac{m^2}{2\mathrm{p}^2},$$

and therefore

$$\boxed{\Delta\phi_{12} \approx \frac{m_1^2 - m_2^2}{2\mathrm{p}}L,} \tag{13.12}$$

where it has been assumed that $T \approx L$ (in natural units), which follows since the neutrino velocity $\beta \approx 1$. At first sight, this treatment appears perfectly reasonable. However, it overlooks that fact that the different mass eigenstates will propagate with different velocities, and therefore will travel the distance L in different times. This objection only can be overcome with a proper wave-packet treatment of the propagation of the coherent state, which yields the same expression as given in

(13.12). However, it is worth noting that the expression of (13.12), which was obtained assuming $\mathrm{p}_1 = \mathrm{p}_2$, also can be obtained by assuming either $E_1 = E_2$ or $\beta_1 = \beta_2$. This can be seen by writing the phase difference of (13.9) as

$$\begin{aligned}\Delta\phi_{12} &= (E_1 - E_2)T - \left(\frac{\mathrm{p}_1^2 - \mathrm{p}_2^2}{\mathrm{p}_1 + \mathrm{p}_2}\right)L \\ &= (E_1 - E_2)T - \left(\frac{E_1^2 - m_1^2 - E_2^2 + m_2^2}{\mathrm{p}_1 + \mathrm{p}_2}\right)L \\ &= (E_1 - E_2)\left[T - \left(\frac{E_1 + E_2}{\mathrm{p}_1 + \mathrm{p}_1}\right)L\right] + \left(\frac{m_1^2 - m_2^2}{\mathrm{p}_1 + \mathrm{p}_2}\right)L. \qquad (13.13)\end{aligned}$$

The first term on the RHS of (13.13) clearly vanishes if it is assumed that $E_1 = E_2$. This term also vanishes if a common velocity is assumed, $\beta_1 = \beta_2 = \beta$ (see Problem 13.1). Hence, although a wave-packet treatment of the neutrino oscillation phenomenon is desirable, it is comforting to see that the same result for the phase difference $\Delta\phi$ is obtained from the assumption of either $\mathrm{p}_1 = \mathrm{p}_2$, $E_1 = E_2$ or $\beta_1 = \beta_2$.

Combining the results of (13.10) and (13.12) and writing $\mathrm{p} = E_\nu$, gives the two-flavour neutrino oscillation probability

$$P(\nu_e \to \nu_\mu) = \sin^2(2\theta)\sin^2\left(\frac{(m_1^2 - m_2^2)L}{4E_\nu}\right). \qquad (13.14)$$

It is convenient to express the oscillation probability in units more suited to the length and energy scales encountered in practice. Writing L in km, Δm^2 in eV^2 and the neutrino energy in GeV, (13.14) can be written

$$P(\nu_e \to \nu_\mu) = \sin^2(2\theta)\sin^2\left(1.27\frac{\Delta m^2[\mathrm{eV}^2]L[\mathrm{km}]}{E_\nu[\mathrm{GeV}]}\right). \qquad (13.15)$$

The corresponding electron neutrino survival probability, $P(\nu_e \to \nu_e)$, either can be obtained from $c_e^* c_e$ or from the conservation of probability, $P(\nu_e \to \nu_e) = 1 - P(\nu_e \to \nu_\mu)$,

$$P(\nu_e \to \nu_e) = 1 - \sin^2(2\theta)\sin^2\left(\frac{(m_1^2 - m_2^2)L}{4E_\nu}\right). \qquad (13.16)$$

Figure 13.12 shows an illustrative example of the oscillation probability as function of distance for $E_\nu = 1\,\mathrm{GeV}$, $\Delta m^2 = 0.002\,\mathrm{eV}^2$ and $\sin^2(2\theta) = 0.8$. The wavelength of the oscillations is given by

$$\lambda_{\mathrm{osc}}[\mathrm{km}] = \frac{\pi E_\nu[\mathrm{GeV}]}{1.27\,\Delta m^2[\mathrm{eV}^2]}.$$

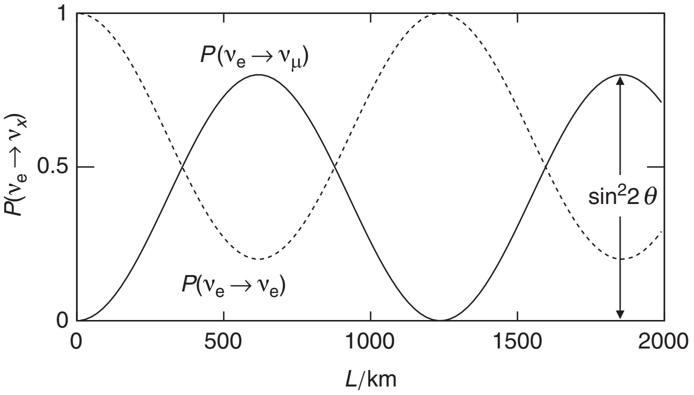

Fig. 13.12 The two-flavour oscillation probability $P(\nu_e \to \nu_\mu)$ and the survival probability $P(\nu_e \to \nu_e)$ plotted as function of L for $E_\nu = 1\,\text{GeV}$, $\Delta m^2 = 0.002\,\text{eV}^2$ and $\sin^2(2\theta) = 0.8$.

For small values of Δm^2, neutrino flavour oscillations only develop over very large distances. This explains why neutrino flavour appeared to be conserved in earlier neutrino experiments. Finally, it should be noted that the amplitude of the oscillations is determined by $\sin^2(2\theta)$, with $\sin^2(2\theta) = 1$ corresponding to maximal mixing.

13.5 Neutrino oscillations of three flavours

The derivation of the neutrino oscillation probability for two flavours contains nearly all of the essential physics, namely the relationship between the weak and mass eigenstates and that the oscillations originate from the phase difference between the mass eigenstates in the time-dependent wavefunction. The full three-flavour derivation of the neutrino oscillation probabilities follows closely the steps above, although the algebra is more involved.

In the three-flavour treatment of neutrino oscillations, the three weak eigenstates are related to the mass eigenstates by the 3×3 unitary Pontecorvo–Maki–Nakagawa–Sakata (PMNS) matrix,

$$\begin{pmatrix} \nu_e \\ \nu_\mu \\ \nu_\tau \end{pmatrix} = \begin{pmatrix} U_{e1} & U_{e2} & U_{e3} \\ U_{\mu 1} & U_{\mu 2} & U_{\mu 3} \\ U_{\tau 1} & U_{\tau 2} & U_{\tau 3} \end{pmatrix} \begin{pmatrix} \nu_1 \\ \nu_2 \\ \nu_3 \end{pmatrix}. \tag{13.17}$$

The elements of the PMNS matrix are fundamental parameters of the lepton flavour sector of the Standard Model. The mass eigenstates can be expressed in terms of the weak eigenstates using the unitarity of the PMNS matrix that implies $U^{-1} = U^\dagger \equiv (U^*)^T$ and hence

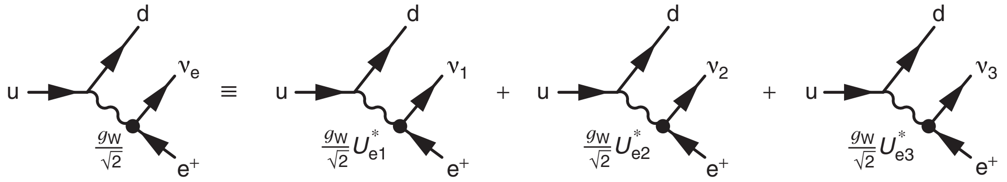

Fig. 13.13 The Feynman diagram for β^+-decay broken down into the contributions from the different mass eigenstates.

$$\begin{pmatrix}\nu_1\\ \nu_2\\ \nu_3\end{pmatrix} = \begin{pmatrix}U^*_{e1} & U^*_{\mu1} & U^*_{\tau1}\\ U^*_{e2} & U^*_{\mu2} & U^*_{\tau2}\\ U^*_{e3} & U^*_{\mu3} & U^*_{\tau3}\end{pmatrix}\begin{pmatrix}\nu_e\\ \nu_\mu\\ \nu_\tau\end{pmatrix}.$$

The unitarity condition, $UU^\dagger = I$, also implies that

$$\begin{pmatrix}U_{e1} & U_{e2} & U_{e3}\\ U_{\mu1} & U_{\mu2} & U_{\mu3}\\ U_{\tau1} & U_{\tau2} & U_{\tau3}\end{pmatrix}\begin{pmatrix}U^*_{e1} & U^*_{\mu1} & U^*_{\tau1}\\ U^*_{e2} & U^*_{\mu2} & U^*_{\tau2}\\ U^*_{e3} & U^*_{\mu3} & U^*_{\tau3}\end{pmatrix} = \begin{pmatrix}1 & 0 & 0\\ 0 & 1 & 0\\ 0 & 0 & 1\end{pmatrix},$$

which gives nine relations between the elements of the PMNS matrix, for example

$$U_{e1}U^*_{e1} + U_{e2}U^*_{e2} + U_{e3}U^*_{e3} = 1, \tag{13.18}$$

$$U_{e1}U^*_{\mu1} + U_{e2}U^*_{\mu2} + U_{e3}U^*_{\mu3} = 0. \tag{13.19}$$

Now consider the neutrino state that is produced in a charged-current weak interaction along with an electron, as indicated in Figure 13.13. The neutrino, which enters the weak interaction vertex as the adjoint spinor, corresponds to a coherent linear superposition of mass eigenstates with a wavefunction at time $t = 0$ of

$$|\psi(0)\rangle = |\nu_e\rangle \equiv U^*_{e1}|\nu_1\rangle + U^*_{e2}|\nu_2\rangle + U^*_{e3}|\nu_3\rangle.$$

The time evolution of the wavefunction is determined by the time evolution of the mass eigenstates and can be written as

$$|\psi(\mathbf{x},t)\rangle = U^*_{e1}|\nu_1\rangle e^{-i\phi_1} + U^*_{e2}|\nu_2\rangle e^{-i\phi_2} + U^*_{e3}|\nu_3\rangle e^{-i\phi_3},$$

where as before $\phi_i = p_i{\cdot}x_i = (E_i t - \mathbf{p}_i{\cdot}\mathbf{x})$ is the phase of the plane wave representing each mass eigenstate. The subsequent *charged-current weak interactions* of the neutrino can be described in terms of its weak eigenstates by writing

$$\begin{aligned}|\psi(\mathbf{x},t)\rangle = {} & U^*_{e1}(U_{e1}|\nu_e\rangle + U_{\mu1}|\nu_\mu\rangle + U_{\tau1}|\nu_\tau\rangle)e^{-i\phi_1}\\ & + U^*_{e2}(U_{e2}|\nu_e\rangle + U_{\mu2}|\nu_\mu\rangle + U_{\tau2}|\nu_\tau\rangle)e^{-i\phi_2}\\ & + U^*_{e3}(U_{e3}|\nu_e\rangle + U_{\mu3}|\nu_\mu\rangle + U_{\tau3}|\nu_\tau\rangle)e^{-i\phi_3}.\end{aligned} \tag{13.20}$$

Because the neutrino appears as the spinor in the weak interaction vertex producing a charged lepton, the mass eigenstates are expressed in terms of the elements of the

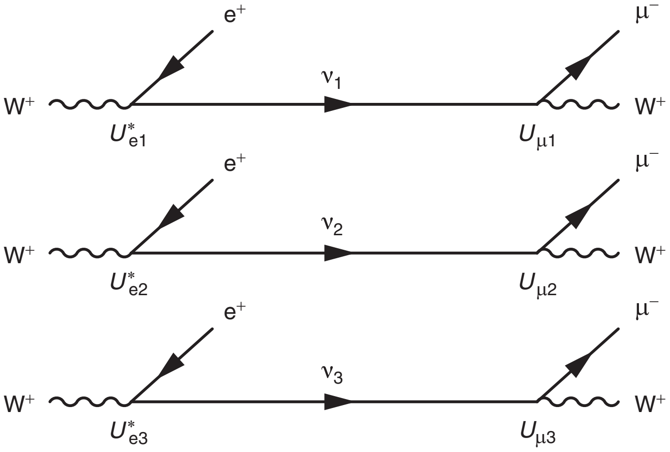

Fig. 13.14 The processes and elements of the PMNS that contribute to $\nu_e \to \nu_\mu$ oscillations.

PMNS matrix and not its complex conjugate. It should be noted that the weak states (ν_e, ν_μ and ν_τ) in (13.20) really refer to the flavour of the lepton produced in a subsequent charged-current weak interaction of the neutrino. Gathering up the terms for each weak eigenstate, Equation (13.20) can be written

$$\begin{aligned} |\psi(\mathbf{x},t)\rangle = \; & (U_{e1}^* U_{e1} e^{-i\phi_1} + U_{e2}^* U_{e2} e^{-i\phi_2} + U_{e3}^* U_{e3} e^{-i\phi_3})|\nu_e\rangle \\ & (U_{e1}^* U_{\mu1} e^{-i\phi_1} + U_{e2}^* U_{\mu2} e^{-i\phi_2} + U_{e3}^* U_{\mu3} e^{-i\phi_3})|\nu_\mu\rangle \\ & (U_{e1}^* U_{\tau1} e^{-i\phi_1} + U_{e2}^* U_{\tau2} e^{-i\phi_2} + U_{e3}^* U_{\tau3} e^{-i\phi_3})|\nu_\tau\rangle. \end{aligned} \tag{13.21}$$

This can be expressed in the form $|\psi(\mathbf{x},t)\rangle = c_e|\nu_e\rangle + c_\mu|\nu_\mu\rangle + c_\tau|\nu_\tau\rangle$, from which the oscillation probabilities can be obtained, for example

$$\begin{aligned} P(\nu_e \to \nu_\mu) &= |\langle\nu_\mu|\psi(\mathbf{x},t)\rangle|^2 = c_\mu c_\mu^* \\ &= |U_{e1}^* U_{\mu1} e^{-i\phi_1} + U_{e2}^* U_{\mu2} e^{-i\phi_2} + U_{e3}^* U_{\mu3} e^{-i\phi_3}|^2. \end{aligned} \tag{13.22}$$

This expression can be understood as the magnitude squared of the sum of the diagrams shown in Figure 13.14, taking into account the relative phase differences that develop over the propagation distance. The oscillation probabilities are defined in terms of the flavours of the *charged* leptons produced in the weak interactions and the relevant PMNS matrix elements. If the phases were all the same, then the complex conjugate of the unitarity relation of (13.19), $U_{e1}^* U_{\mu1} + U_{e2}^* U_{\mu2} + U_{e3}^* U_{\mu3} = 0$, would imply $P(\nu_e \to \nu_\mu) = 0$ and, as before, neutrino flavour oscillations only occur if the neutrinos have mass, and the masses are not all the same.

Equation (13.22) can be simplified using the complex number identity,

$$|z_1 + z_2 + z_3|^2 \equiv |z_1|^2 + |z_2|^2 + |z_3|^2 + 2\,\Re\mathrm{e}\{z_1 z_2^* + z_1 z_3^* + z_2 z_3^*\}, \tag{13.23}$$

giving

$$P(\nu_e \to \nu_\mu) = |U_{e1}^* U_{\mu 1}|^2 + |U_{e2}^* U_{\mu 2}|^2 + |U_{e3}^* U_{\mu 3}|^2 + 2\,\Re\mathrm{e}\{U_{e1}^* U_{\mu 1} U_{e2} U_{\mu 2}^* e^{-i(\phi_1-\phi_2)}\}$$
$$+ 2\,\Re\mathrm{e}\{U_{e1}^* U_{\mu 1} U_{e3} U_{\mu 3}^* e^{-i(\phi_1-\phi_3)}\} + 2\,\Re\mathrm{e}\{U_{e2}^* U_{\mu 2} U_{e3} U_{\mu 3}^* e^{-i(\phi_2-\phi_3)}\}. \tag{13.24}$$

This can be simplified further by applying the identity (13.23) to the modulus squared of the complex conjugate of the unitarity relation of (13.19), which gives

$$|U_{e1}^* U_{\mu 1}|^2 + |U_{e2}^* U_{\mu 2}|^2 + |U_{e3}^* U_{\mu 3}|^2 +$$
$$2\,\Re\mathrm{e}\{U_{e1}^* U_{\mu 1} U_{e2} U_{\mu 2}^* + U_{e1}^* U_{\mu 1} U_{e3} U_{\mu 3}^* + U_{e2}^* U_{\mu 2} U_{e3} U_{\mu 3}^*\} = 0,$$

and thus, (13.24) can be written as

$$P(\nu_e \to \nu_\mu) = 2\,\Re\mathrm{e}\{U_{e1}^* U_{\mu 1} U_{e2} U_{\mu 2}^* [e^{i(\phi_2-\phi_1)} - 1]\}$$
$$2\,\Re\mathrm{e}\{U_{e1}^* U_{\mu 1} U_{e3} U_{\mu 3}^* [e^{i(\phi_3-\phi_1)} - 1]\}$$
$$2\,\Re\mathrm{e}\{U_{e2}^* U_{\mu 2} U_{e3} U_{\mu 3}^* [e^{i(\phi_3-\phi_2)} - 1]\}. \tag{13.25}$$

The electron neutrino survival probability $P(\nu_e \to \nu_e)$ can be obtained in a similar manner starting from (13.24) and using the unitarity relation of (13.18). In this case, each element of the PMNS matrix is paired with the corresponding complex conjugate, e.g. $U_{e1}U_{e1}^*$, and the combinations of PMNS matrix elements give real numbers. Therefore, the electron neutrino survival probability is

$$P(\nu_e \to \nu_e) = 1 + 2|U_{e1}|^2|U_{e2}|^2\,\Re\mathrm{e}\{[e^{i(\phi_2-\phi_1)} - 1]\}$$
$$+ 2|U_{e1}|^2|U_{e3}|^2\,\Re\mathrm{e}\{[e^{i(\phi_3-\phi_1)} - 1]\}$$
$$+ 2|U_{e2}|^2|U_{e3}|^2\,\Re\mathrm{e}\{[e^{i(\phi_3-\phi_2)} - 1]\}. \tag{13.26}$$

Equation (13.26) can be simplified by noting

$$\Re\mathrm{e}\{e^{i(\phi_j-\phi_i)} - 1\} = \cos(\phi_j - \phi_i) - 1 = -2\sin^2\left(\frac{\phi_j - \phi_i}{2}\right) = -2\sin^2\Delta_{ji},$$

where Δ_{ji} is defined as

$$\Delta_{ji} = \frac{\phi_j - \phi_i}{2} = \frac{(m_j^2 - m_i^2)L}{4E_\nu}.$$

Hence, (13.26) can be written

$$P(\nu_e \to \nu_e) = 1 - 4|U_{e1}|^2|U_{e2}|^2\sin^2\Delta_{21}$$
$$- 4|U_{e1}|^2|U_{e3}|^2\sin^2\Delta_{31} - 4|U_{e2}|^2|U_{e3}|^2\sin^2\Delta_{32}. \tag{13.27}$$

The electron neutrino survival probability depends on three differences of squared masses, $\Delta m^2_{21} = m^2_2 - m^2_1$, $\Delta m^2_{31} = m^2_3 - m^2_1$ and $\Delta m^2_{32} = m^2_3 - m^2_2$. Only two of these differences are independent and Δ_{31} can be expressed as

$$\Delta_{31} = \Delta_{32} + \Delta_{21}. \tag{13.28}$$

Before using the above formulae to describe the experimental data, it is worth discussing the current knowledge of neutrino masses, the nature of the PMNS matrix and the discrete symmetries related to the neutrino oscillation phenomena, including the possibility of CP violation.

13.5.1 Neutrino masses and the neutrino mass hierarchy

Since the neutrino oscillation probabilities depend on differences of the squared neutrino masses, the experimental measurements of neutrino oscillations do not constrain the overall neutrino mass scale. To date, there are no direct measurements of neutrino masses, only upper limits. From studies of the end point of the electron energy distribution in the nuclear β-decay of tritium, it is known that the mass of the lightest neutrino is $\lesssim 2\,\mathrm{eV}$. Tighter, albeit model-dependent, limits can be obtained from cosmology. The density of low-energy relic neutrinos from the Big Bang is large, $\mathcal{O}(100)\,\mathrm{cm}^{-3}$ for each flavour. Consequently, neutrino masses potentially impact the evolution of the Universe. From recent cosmological measurements of the large-scale structure of the Universe, it can be deduced that

$$\sum_{i=1}^{3} m_{\nu_i} \lesssim 1\,\mathrm{eV}.$$

Whilst the neutrino masses are not known, it is clear that they are much smaller than those of either the charged leptons or the quarks. Even with neutrino masses at the eV scale, they are smaller by a factor of at least 10^6 than the mass of the electron and smaller by a factor of at least 10^9 than the mass of the tau-lepton. The current hypothesis for this large difference, known as the seesaw mechanism, is discussed in Chapter 17.

The results of recent neutrino oscillation experiments, which are described in Sections 13.7 and 13.8, provide determinations of differences of the squares of the neutrino masses

$$\Delta m^2_{21} = m^2_2 - m^2_1 \approx 8 \times 10^{-5}\,\mathrm{eV}^2,$$
$$|\Delta m^2_{32}| = |m^2_3 - m^2_2| \approx 2 \times 10^{-3}\,\mathrm{eV}^2.$$

Regardless of the absolute mass scale of the lightest neutrino, there are two possible hierarchies for the neutrino masses, shown in Figure 13.15. In the *normal* hierarchy $m_3 > m_2$ and in the *inverted* mass hierarchy $m_3 < m_2$. Current experiments

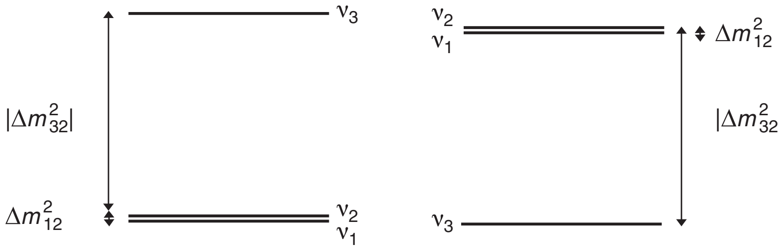

Fig. 13.15 The two possible neutrino mass hierarchies, normal where $m_3 > m_2$ and inverted where $m_2 > m_3$.

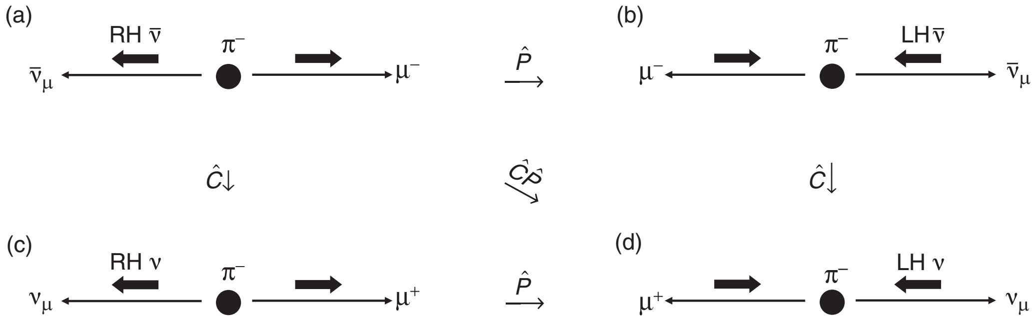

Fig. 13.16 The effect of parity, charge-conjugation and combined CP operation on pion decay.

are not sensitive enough to distinguish between these two possibilities. However, regardless of the hierarchy, because $\Delta m^2_{21} \ll |\Delta m^2_{32}|$ in most circumstances it is reasonable to make the approximation

$$|\Delta m^2_{31}| \approx |\Delta m^2_{32}|.$$

13.5.2 CP violation in neutrino oscillations

The $V - A$ chiral structure of the weak charged-current implies that parity is maximally violated. It also implies that charge-conjugation symmetry is maximally violated. This can be seen by considering the weak decay $\pi^- \to \mu^- \bar{\nu}_\mu$. Because neutrino masses are extremely small compared to the energies involved, the antineutrino is effectively always emitted in a RH helicity state, as shown in Figure 13.16a. The effect of the parity operator, shown in Figure 13.16b, is to reverse the particle momenta leaving the particle spins (axial-vectors) unchanged. The result of the parity transformation is a final state with a LH antineutrino, for which the weak charged-current matrix element is zero.

The effect of the charge conjugation operator $\hat{C}$ is to replace particles by their antiparticles and *vice versa*, is shown in Figure 13.16c. Charge conjugation results in a RH neutrino in the final state. Since only LH particle states participate in the weak interaction, the matrix element for this process is also zero. Thus the weak interaction maximally violates charge-conjugation symmetry. The combined effect of C and P, shown in Figure 13.16d, results in a valid weak decay involving a LH neutrino. For this reason it is plausible that the weak interaction respects the combined CP symmetry.

It is known that CP violation is needed to account for the excess of matter over antimatter in the Universe today (see Chapter 14). Since the QED and QCD interactions conserve C and P separately, and therefore conserve CP, the only possible place in the Standard Model where CP-violating effects can occur is in the weak interaction.

Time reversal symmetry and CPT

Parity is a discrete symmetry operation corresponding to $\mathbf{x} \to -\mathbf{x}$. Similarly, time reversal is a discrete symmetry operation that has the effect $t \to -t$. Following the arguments of Chapter 11, it should be clear that the vector nature of the QED and QCD interactions, implies that the matrix elements of QED and QCD are invariant under time reversal. More generally, all local Lorentz-invariant Quantum Field Theories can be shown to be invariant under the combined operation of C, P and T. One consequence of this CPT symmetry is that particles and antiparticles have identical masses, magnetic moments, etc. The best experimental limit on CPT invariance comes from the equality of the masses of the flavour eigenstates of the neutral kaons, $\mathrm{K}^0(\mathrm{d}\overline{\mathrm{s}})$ and $\overline{\mathrm{K}}^0(\mathrm{s}\overline{\mathrm{d}})$, where

$$\frac{|m(\mathrm{K}^0) - m(\overline{\mathrm{K}}^0)|}{m(\mathrm{K}^0)} < 10^{-18}.$$

CPT is believed to be an exact symmetry of the Universe. This implies that, if physics is unchanged by the combined operation of C and P, then time reversal symmetry also holds. The corollary is that CP violation implies that T reversal symmetry is also violated and vice versa.

CP and T violation in neutrino oscillations

It is instructive to consider the effects of the discrete symmetry transformations, CP, T and CPT, in the context of neutrino oscillations. If time reversal symmetry applies, then the oscillation probability for $P(\nu_e \to \nu_\mu)$ will be equal to $P(\nu_\mu \to \nu_e)$. The oscillation probability $P(\nu_e \to \nu_\mu)$ is given by (13.25)

$$P(\nu_e \to \nu_\mu) = 2\,\Re e\{U_{e1}^* U_{\mu 1} U_{e2} U_{\mu 2}^* [e^{i(\phi_2 - \phi_1)} - 1]\} + \cdots . \tag{13.29}$$

The corresponding expression for the oscillation probability $P(\nu_\mu \to \nu_e)$ is obtained by swapping the e and μ labels

$$P(\nu_\mu \to \nu_e) = 2\,\Re e\{U_{\mu 1}^* U_{e1} U_{\mu 2} U_{e2}^* [e^{i(\phi_2 - \phi_1)} - 1]\} + \cdots .$$

The elements of the PMNS matrix that appear in the expression for $P(\nu_\mu \to \nu_e)$ are the complex conjugates of those in the expression for $P(\nu_e \to \nu_\mu)$. Hence, unless all elements U_{ei} and $U_{\mu j}$ are real, time reversal symmetry does not necessarily hold in neutrino oscillations, which in turn implies the possibility of CP violation.

The effect of the CP operation on $\nu_e \to \nu_\mu$ flavour transformations is

$$\nu_e \to \nu_\mu \quad \xrightarrow{\hat{C}\hat{P}} \quad \overline{\nu}_e \to \overline{\nu}_\mu,$$

where C transforms particles in to antiparticles and P ensures that the LH neutrinos transform to RH antineutrinos. The oscillation probability $P(\overline{\nu}_e \to \overline{\nu}_\mu)$ can be obtained from that for $P(\nu_e \to \nu_\mu)$ by noting that whether the element of the PMNS matrix appears as U or U^* depends on whether the neutrino appears as the spinor or adjoint spinor in the weak interaction vertex (see Section 13.3.1). Consequently

$$P(\overline{\nu}_e \to \overline{\nu}_\mu) = 2\,\Re e\{U_{e1}U^*_{\mu 1}U^*_{e2}U_{\mu 2}[e^{i(\phi_2-\phi_1)} - 1]\} + \cdots .$$

Again, unless all the elements U_{ei} and $U_{\mu j}$ are real, $P(\nu_e \to \nu_\mu) \neq P(\overline{\nu}_e \to \overline{\nu}_\mu)$, and CP can be violated in neutrino oscillations. Finally, consider the combined CPT operation

$$\nu_e \to \nu_\mu \quad \xrightarrow{\hat{C}\hat{P}\hat{T}} \quad \overline{\nu}_\mu \to \overline{\nu}_e,$$

where the effect of time reversal swaps the e and μ labels and the effect CP is to exchange $U \leftrightarrow U^*$ and therefore

$$P(\overline{\nu}_\mu \to \overline{\nu}_e) = 2\,\Re e\{U_{\mu 1}U^*_{e1}U^*_{\mu 2}U_{e2}[e^{i(\phi_2-\phi_1)} - 1]\} + \cdots = P(\nu_e \to \nu_\mu).$$

As expected, neutrino oscillations are invariant under the combined action of CPT.

The imaginary components of the PMNS matrix, provide a possible source of CP violation in the Standard Model. The relative magnitude of the CP violation in neutrino oscillations is given by $P(\nu_e \to \nu_\mu) - P(\overline{\nu}_e \to \overline{\nu}_\mu)$. This can be shown to be (see Problem 13.4)

$$P(\nu_e \to \nu_\mu) - P(\overline{\nu}_e \to \overline{\nu}_\mu) = 16\,\Im m\{U^*_{e1}U_{\mu 1}U_{e2}U^*_{\mu 2}\}\sin\Delta_{12}\sin\Delta_{13}\sin\Delta_{23}. \tag{13.30}$$

With the current experimental knowledge of the PMNS matrix elements, it is known that the difference $P(\nu_e \to \nu_\mu) - P(\overline{\nu}_e \to \overline{\nu}_\mu)$ is at most a few percent. CP violating effects in neutrino oscillations are small and are beyond the sensitivity of the current generation of experiments.

The PMNS matrix

In the Standard Model, the unitarity PMNS matrix can be described in terms of three real parameters and a single phase. The reasoning is subtle. A general 3 × 3 matrix can be described by nine complex numbers. The unitarity of the PMNS matrix, $UU^\dagger = I$, provides nine constraints, leaving nine independent parameters. If the PMNS matrix were real, it would be correspond to the orthogonal rotation matrix R and could be described by three rotation angles, θ_{12}, θ_{13} and θ_{23}

$$R = \begin{pmatrix} 1 & 0 & 0 \\ 0 & c_{23} & s_{23} \\ 0 & -s_{23} & c_{23} \end{pmatrix} \times \begin{pmatrix} c_{13} & 0 & s_{13} \\ 0 & 1 & 0 \\ -s_{13} & 0 & c_{13} \end{pmatrix} \times \begin{pmatrix} c_{12} & s_{12} & 0 \\ -s_{12} & c_{12} & 0 \\ 0 & 0 & 1 \end{pmatrix}, \tag{13.31}$$

where $s_{ij} = \sin\theta_{ij}$ and $c_{ij} = \cos\theta_{ij}$. In this form θ_{12} is the angle of rotation about the three-axis, θ_{13} is the angle of rotation about the new two-axis, and θ_{23} is a rotation about the resulting one-axis.

Since the PMNS matrix is unitary, not real, there are six additional degrees of freedom that appear as complex phases of the form $\exp(i\delta)$. It turns out that not all of these phases are physically relevant. This can be seen by writing the currents for the possible leptonic weak interaction charged-current vertices as

$$-i\frac{g_W}{\sqrt{2}}\,(\bar{\mathrm{e}}, \bar{\mu}, \bar{\tau})\,\gamma^\mu \tfrac{1}{2}(1-\gamma^5) \begin{pmatrix} U_{e1} & U_{e2} & U_{e3} \\ U_{\mu 1} & U_{\mu 2} & U_{\mu 3} \\ U_{\tau 1} & U_{\tau 2} & U_{\tau 3} \end{pmatrix} \begin{pmatrix} \nu_1 \\ \nu_2 \\ \nu_3 \end{pmatrix}.$$

These four-vector currents are unchanged by the transformation,

$$\ell_\alpha \to \ell_\alpha e^{i\theta_\alpha}, \quad \nu_k \to \nu_k e^{i\theta_k} \quad \text{and} \quad U_{\alpha k} \to U_{\alpha k} e^{i(\theta_\alpha - \theta_k)}, \tag{13.32}$$

where ℓ_α is the charged lepton of type $\alpha = \mathrm{e}, \mu, \tau$. Hence, it might appear that the six complex phases in the PMNS matrix can be absorbed into the definitions of the phases of the neutrino and charged leptons without any physical consequences. This is not the case because an overall phase factor in the PMNS matrix multiplying all elements has no physical consequence. For this reason, it is possible to pull out a common phase $U \to Ue^{i\theta}$. In this way all phases can be defined relative to, for example, the phase of the electron θ_e such that $\theta_k = \theta_e + \theta'_k$. In this case the transformation of (13.32) becomes

$$\ell_\alpha \to \ell_\alpha e^{i(\theta_e + \theta'_\alpha)}, \quad \nu_k \to \nu_k e^{i(\theta_e + \theta'_k)} \quad \text{and} \quad U_{\alpha k} \to U_{\alpha k} e^{i(\theta'_\alpha - \theta'_k)},$$

from which it can be seen that only five phases of the PMNS matrix can be absorbed into the definition of the particles since $\theta'_e = 0$ and the common phase $e^{i\theta_e}$ has no physical consequences. Hence the PMNS matrix can be expressed in terms of three mixing angles, θ_{12}, θ_{23} and θ_{13} and a single complex phase δ.

The PMNS matrix is usually written as

$$U_{\mathrm{PMNS}} = \begin{pmatrix} U_{e1} & U_{e2} & U_{e3} \\ U_{\mu 1} & U_{\mu 2} & U_{\mu 3} \\ U_{\tau 1} & U_{\tau 2} & U_{\tau 3} \end{pmatrix} = \begin{pmatrix} 1 & 0 & 0 \\ 0 & c_{23} & s_{23} \\ 0 & -s_{23} & c_{23} \end{pmatrix} \begin{pmatrix} c_{13} & 0 & s_{13}e^{-i\delta} \\ 0 & 1 & 0 \\ -s_{13}e^{i\delta} & 0 & c_{13} \end{pmatrix} \begin{pmatrix} c_{12} & s_{12} & 0 \\ -s_{12} & c_{12} & 0 \\ 0 & 0 & 1 \end{pmatrix}.$$

This form is particularly convenient because θ_{13} is known to be relatively small and thus the central matrix is almost diagonal. The individual elements of the PMNS matrix, obtained from the matrix multiplication, are

$$\begin{pmatrix} U_{e1} & U_{e2} & U_{e3} \\ U_{\mu 1} & U_{\mu 2} & U_{\mu 3} \\ U_{\tau 1} & U_{\tau 2} & U_{\tau 3} \end{pmatrix} = \begin{pmatrix} c_{12}c_{13} & s_{12}c_{13} & s_{13}e^{-i\delta} \\ -s_{12}c_{23} - c_{12}s_{23}s_{13}e^{i\delta} & c_{12}c_{23} - s_{12}s_{23}s_{13}e^{i\delta} & s_{23}c_{13} \\ s_{12}s_{23} - c_{12}c_{23}s_{13}e^{i\delta} & -c_{12}s_{23} - s_{12}c_{23}s_{13}e^{i\delta} & c_{23}c_{13} \end{pmatrix}. \tag{13.33}$$

It is worth noting that, in the two-flavour treatment of neutrino oscillations, the general form of the unitary transformation between weak and mass eigenstates has four parameters, a rotation angle and three complex phases. But, all three complex phases can be absorbed into the definitions of the particles, and the resulting matrix depends on a single angle, as assumed in (13.6). In this case the matrix is entirely real and therefore cannot accommodate the CP violation. Hence CP violation originating from the PMNS matrix occurs only for three or more generations of leptons.

13.6 Neutrino oscillation experiments

Early experimental results on neutrino oscillations were obtained from studies of solar neutrinos and the neutrinos produced in cosmic-ray-induced cascades in the atmosphere. More recent results have been obtained from long-baseline neutrino oscillation beam experiments and from the study of electron antineutrinos from nuclear fission reactors. There are two possible signatures for neutrino oscillations. Firstly neutrino oscillations can result in the *appearance* of "wrong" flavour charged leptons, for example the observation of e^- and/or τ^- from an initially pure beam of ν_μ. Alternatively, neutrino oscillations can be observed as the *disappearance* of the "right" flavour charged lepton, where fewer than expected μ^- are produced from an initially pure ν_μ beam.

13.6.1 Neutrino interaction thresholds

The observable experimental effects resulting from neutrino oscillations depend on the type of neutrino interactions that are detectable. Neutrinos can be detected in matter through their charged-current and neutral-current weak interactions, either with atomic electrons or with nucleons, as shown in Figure 13.17. Unless kinematically forbidden, interactions with nucleons will dominate, since the neutrino interaction cross sections are proportional to the centre-of-mass energy squared, $s \approx 2mE_\nu$, where m is the mass of the target particle (see for example, Section 12.3).

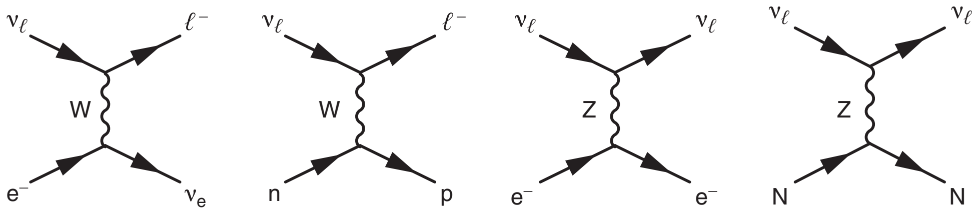

Fig. 13.17 The Feynman diagrams for CC and NC neutrino interactions in matter. For $\overline{\nu}_e$ there is also an s-channel process, $\overline{\nu}_e e^- \to \overline{\nu}_e e^-$.

Whether an appearance signal can be observed depends on whether the interaction is kinematically allowed. Charged-current neutrino interactions are allowed if the centre-of-mass energy is sufficient to produce a charged lepton and the final-state hadronic system. The threshold is determined by the lowest W^2 process, $\nu_\ell n \to \ell^- p$. In the laboratory frame, where the neutron is at rest, the centre-of-mass energy squared is given by

$$s = (p_\nu + p_n)^2 = (E_\nu + m_n)^2 - E_\nu^2 = 2E_\nu m_n + m_n^2.$$

The $\nu_\ell n \to \ell^- p$ interaction is only kinematically allowed if $s > (m_\ell + m_p)^2$,

$$E_\nu > \frac{(m_p^2 - m_n^2) + m_\ell^2 + 2m_p m_\ell}{2m_n}.$$

From this expression, the laboratory frame neutrino threshold energies for charged-current interactions with a nucleon are

$$E_{\nu_e} > 0, \quad E_{\nu_\mu} > 110\,\text{MeV} \quad \text{and} \quad E_{\nu_\tau} > 3.5\,\text{GeV}.$$

For electron neutrinos with energies of order a few MeV, the nuclear binding energy also has to be taken into account.

Charged-current interactions with an atomic electron $\nu_\ell e^- \to \nu_e \ell^-$ are kinematically allowed if $s > m_\ell^2$, where m_ℓ is the mass of the final-state charged lepton. In the laboratory frame

$$s = (p_\nu + p_e)^2 = (E_\nu + m_e)^2 - E_\nu^2 = 2E_\nu m_e + m_e^2,$$

and hence

$$E_\nu > \frac{m_\ell^2 - m_e^2}{2m_e},$$

leading to laboratory frame thresholds for charged-current νe^- scattering of

$$E_{\nu_e} > 0, \quad E_{\nu_\mu} > 11\,\text{GeV} \quad \text{and} \quad E_{\nu_\tau} > 3090\,\text{GeV}.$$

Consequently, for the neutrino energies encountered in most experiments, interactions with atomic electrons are relevant only for electron neutrinos/antineutrinos.

13.7 Reactor experiments

Nuclear fission reactors produce a large flux of electron antineutrinos from the β-decays of radioisotopes such as ^{235}U, ^{238}U, ^{239}Pu and ^{241}Pu, which are produced in nuclear fission. The mean energy of the reactor antineutrinos is about 3 MeV and the flux is known precisely from the power produced by the reactor (which is closely monitored). The $\overline{\nu}_e$ can be detected through the inverse β-decay process,

$$\overline{\nu}_e + p \to e^+ + n.$$

If the $\overline{\nu}_e$ oscillate to other neutrino flavours, they will not be detected since the neutrino energy is well below threshold to produce a muon or tau-lepton the final state. Hence it is only possible to observe the disappearance of reactor $\overline{\nu}_e$. The $\overline{\nu}_e$ survival probability is given by (13.27), which with the approximation $\Delta_{31} \approx \Delta_{32}$ becomes

$$P(\overline{\nu}_e \to \overline{\nu}_e) \approx 1 - 4|U_{e1}|^2|U_{e2}|^2 \sin^2 \Delta_{21} - 4|U_{e3}|^2 \left[|U_{e1}|^2 + |U_{e2}|^2\right] \sin^2 \Delta_{32}.$$

Using the unitarity relation of (13.18), this can be written as

$$P(\overline{\nu}_e \to \overline{\nu}_e) \approx 1 - 4|U_{e1}|^2|U_{e2}|^2 \sin^2 \Delta_{21} - 4|U_{e3}|^2 \left[1 - |U_{e3}|^2\right] \sin^2 \Delta_{32}, \tag{13.34}$$

which can be expressed in terms of the PMNS matrix elements of (13.33) as

$$\begin{aligned} P(\overline{\nu}_e \to \overline{\nu}_e) &= 1 - 4(c_{12}c_{13})^2(s_{12}c_{13})^2 \sin^2 \Delta_{21} - 4s_{13}^2(1 - s_{13}^2) \sin^2 \Delta_{32} \\ &= 1 - \cos^4(\theta_{13}) \sin^2(2\theta_{12}) \sin^2\left(\frac{\Delta m_{21}^2 L}{4E_{\overline{\nu}}}\right) - \sin^2(2\theta_{13}) \sin^2\left(\frac{\Delta m_{32}^2 L}{4E_{\overline{\nu}}}\right). \end{aligned} \tag{13.35}$$

Figure 13.18 shows the expected $\overline{\nu}_e$ survival probability assuming $\theta_{12} = 30°$, $\theta_{23} = 45°$, $\theta_{13} = 10°$ and

$$\Delta m_{21}^2 = 8 \times 10^{-5}\,\text{eV}^2 \quad \text{and} \quad \Delta m_{32}^2 = 2.5 \times 10^{-3}\,\text{eV}^2.$$

The oscillations occur on two different length scales. The short wavelength component, which depends on Δm_{32}^2, oscillates with an amplitude of $\sin^2(2\theta_{13})$ about the longer wavelength component, with wavelength determined by Δm_{21}^2. Hence, measurements of the $\overline{\nu}_e$ survival probability at distances of $O(1)$ km are sensitive to θ_{13} and measurements at distances of $O(100)$ km are sensitive to Δm_{21}^2 and θ_{12}.

13.7.1 The short-baseline reactor experiments

Close to a fission reactor, where the long wavelength contribution to neutrino oscillations has yet to develop, the electron antineutrino survival probability of (13.35) can be approximated by

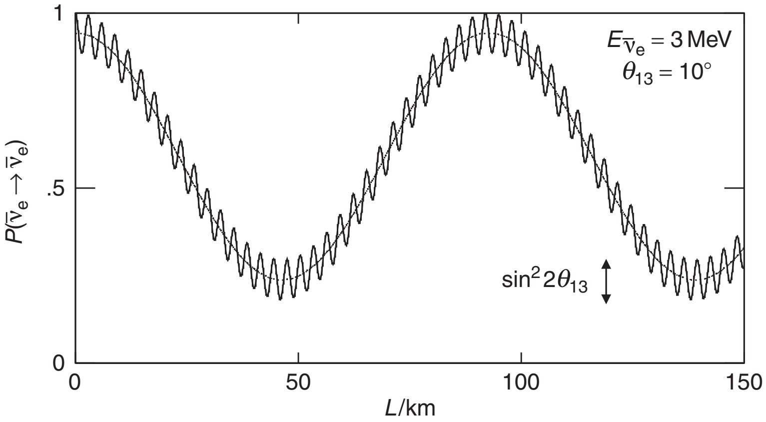

Fig. 13.18 The $P(\overline{\nu}_e \to \overline{\nu}_e)$ survival probability as a function of distance for 3 MeV $\overline{\nu}_e$ assuming $\theta_{13} = 10°$.

$$P(\overline{\nu}_e \to \overline{\nu}_e) \approx 1 - \sin^2(2\theta_{13})\sin^2\left(\frac{\Delta m^2_{32} L}{4E_{\overline{\nu}}}\right). \qquad (13.36)$$

Until recently, such short-baseline neutrino oscillations had not been observed, and θ_{13} only was known to be small. The first conclusive observations of a non-zero value of θ_{13} were published in 2012.

The Daya Bay experiment in China detects neutrinos from six reactor cores each producing 2.9 GW of power. The experiment consists of six detectors, two at a mean flux-weighted distance of 470 m from the reactors, one at 576 m and three at 1.65 km. Each detector consists of a large vessel containing 20 tons of liquid scintillator loaded with gadolinium. The vessels are viewed by arrays of photomultiplier tubes. Electron antineutrinos are detected by the inverse β-decay reaction $\overline{\nu}_e + p \to e^+ + n$. The subsequent annihilation of the positron with an electron gives two *prompt* photons. The low-energy neutron scatters in the liquid scintillator until it is captured by a gadolinium nucleus. The neutron capture, which occurs on a timescale of 100 μs, produces photons from $n + \text{Gd} \to \text{Gd}^* \to \text{Gd} + \gamma$. The photons from both the annihilation process and neutron capture produce Compton scattered electrons. These electrons then ionise the liquid scintillator producing scintillation light. The signature for a $\overline{\nu}_e$ interaction is therefore the coincidence of a prompt pulse of scintillation light from the annihilation and a delayed pulse from the neutron capture 10–100 μs later. The observed amount of prompt light provides a measure of the neutrino energy.

The signal for neutrino oscillations at Daya Bay is a deficit of antineutrinos that depends on the distance from the reactors and a distortion of the observed e^+ energy spectrum. By comparing the data recorded in the three *far* detectors at 1.65 km from the reactors, with the data from the three *near* detectors, many systematic uncertainties cancel. In the absence of neutrino oscillations, the rates in the near and far detectors will be compatible and the same energy distribution

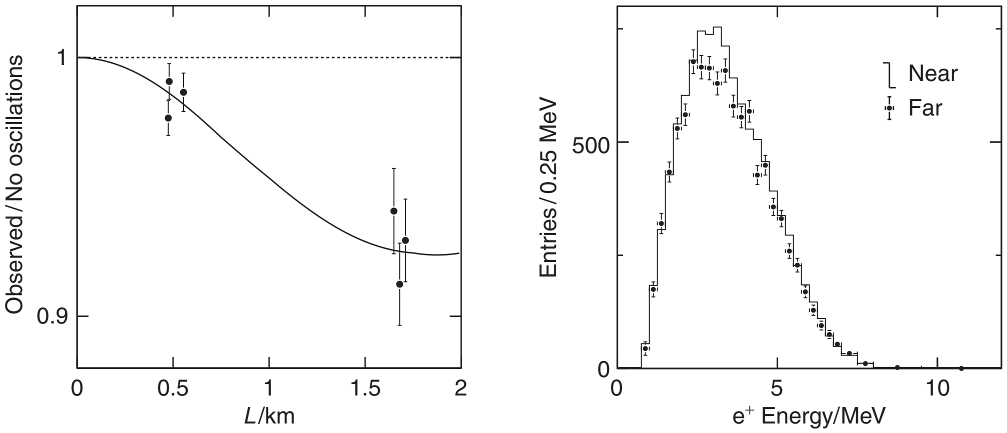

Fig. 13.19 Left: the observed antineutrino rates in the Daya Bay experiment scaled to the expectation for no oscillations, plotted as a function of the flux-weighted distance to the reactors. Right: the observed background-subtracted e^+ energy spectrum in the far detectors compared to the corresponding scaled distributions from the near detectors. Adapted from An *et al.* (2012).

will be observed in all detectors. The left-hand plot of Figure 13.19 shows the observed background-subtracted rates in the near and far detectors relative to the unoscillated expectation. The results show a clear deficit of events compared to the unoscillated expectation and this deficit increases with the distance from the reactors. Accounting for scaling of the fluxes with distance, the observed ratio of far/near rates is

$$N_{\text{far}}/N_{\text{near}} = 0.940 \pm 0.012.$$

The right-hand plot of Figure 13.19 shows the observed e^+ energy spectrum in the far detectors compared to that in the near detectors, scaled to the same integrated neutrino flux. A clear difference is observed, with the maximum deficit in the far detectors occurring in the 2–4 MeV range, consistent with neutrino oscillations with the known value of $\Delta m^2_{32} = 2.3 \times 10^{-3}\,\text{eV}^2$ (see Section 13.8). The observed ratio of far-to-near event rates gives $\sin^2(2\theta_{13}) = 0.092 \pm 0.017$.

Recent results from the RENO reactor experiment in South Korea, which is similar in design to the Daya Bay experiment, also show a deficit of electron antineutrinos, compatible with $\sin^2(2\theta_{13}) = 0.113 \pm 0.023$, see Ahn *et al.* (2012). Based on the initial Daya Bay and RENO results, it can be concluded that

$$\boxed{\sin^2(2\theta_{13}) \simeq 0.10 \pm 0.01.}$$

Further, albeit less significant, evidence for a non-zero value of θ_{13} has been provided by the Double-Chooz, MINOS and T2K experiments.

13.7.2 The KamLAND experiment

The KamLAND experiment, located in the same mine as the Super-Kamiokande experiment, detected $\overline{\nu}_e$ from a number of reactors (with a total power 70 GW) located at distances in the range 130–240 km from the detector. The KamLAND detector consisted of a large volume of liquid scintillator surrounded by almost 1800 PMTs. Antineutrinos are again detected by the inverse β-decay reaction, $\overline{\nu}_e + p \to e^+ + n$, giving a prompt signal from the positron annihilation followed by a delayed signal from the 2.2 MeV photon produced from the neutron capture reaction, $n + p \to D + \gamma$. At the distances relevant to the KamLAND experiment, the L/E dependence of the rapid oscillations due to the Δm^2_{32} term in (13.35) is not resolved because the neutrino sources (the reactors) are not at a single distance L and also because the energy resolution is insufficient to resolve the rapid neutrino energy dependence. Consequently, only the average value of

$$\langle \sin^2 \Delta_{32} \rangle = \tfrac{1}{2},$$

is relevant. Therefore the survival probability of (13.35) can be written

$$\begin{aligned} P(\overline{\nu}_e \to \overline{\nu}_e) &= 1 - \cos^4(\theta_{13}) \sin^2(2\theta_{12}) \sin^2 \Delta_{21} - \tfrac{1}{2} \sin^2(2\theta_{13}) \\ &= \cos^4(\theta_{13}) + \sin^4(\theta_{13}) - \cos^4(\theta_{13}) \sin^2(2\theta_{12}) \sin^2 \Delta_{21}. \end{aligned}$$

Neglecting the $\sin^4(\theta_{13})$ term, which is small (< 0.001), gives

$$P(\overline{\nu}_e \to \overline{\nu}_e) \approx \cos^4(\theta_{13}) \left[1 - \sin^2(2\theta_{12}) \sin^2 \left(\frac{\Delta m^2_{21} L}{4 E_{\overline{\nu}}} \right) \right]. \tag{13.37}$$

Hence, the effective survival probability for reactor neutrinos at large distances has the same form as the two-flavour oscillation formula multiplied by $\cos^4(\theta_{13}) \approx 0.95$.

The KamLAND experiment observed 1609 reactor $\overline{\nu}_e$ interactions compared to the expectation of 2179±89 in the absence of neutrino oscillations. For each event, a measurement of the neutrino energy was obtained from the amount of light associated with the prompt scintillation signal from the positron annihilation. By comparing the energy distribution of the observed data with the expected distribution, the survival probability can be plotted as a function of $L_0/E_{\overline{\nu}}$, where $L_0 = 180$ km is the flux-weighted average distance to the reactors contributing to $\overline{\nu}_e$ interactions in KamLAND, as shown in Figure 13.20. The range of L/E sampled is determined by the energies of the neutrinos produced in nuclear reactors, ~2–7 MeV. The data show a clear oscillation signal with a decrease and subsequent rise in the mean oscillation probability. The measured distribution can be compared to the expectation of (13.37) after accounting for the experimental energy resolution and range of distances sampled, which smears out the effect of the oscillations.

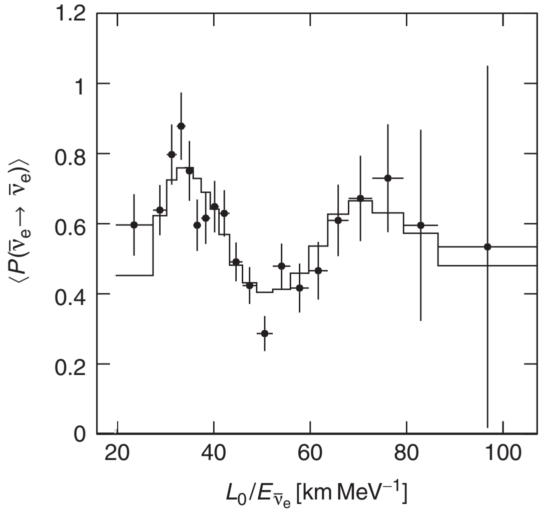

Fig. 13.20 KamLAND data showing the measured mean survival probability as a function of the measured neutrino energy divided by the flux-weighted mean distance to the reactors, L_0. The histogram shows the expected distribution for the oscillation parameters that best describe the data. Adapted from Abe *et al.* (2008).

The location of the minimum at $L_0/E_{\bar{\nu}_e} \sim 50\,\text{km MeV}^{-1}$ provides a tight constraint on $\Delta m^2_{21} = m^2_2 - m^2_1$,

$$\Delta m^2_{21} = (7.6 \pm 0.2) \times 10^{-5}\,\text{eV}^2.$$

A measurement of the mixing angle θ_{12} can also be obtained, which when combined with the more precise determination from the solar neutrino data of SNO (see Section 13.2) gives

$$\sin^2(2\theta_{12}) = 0.87 \pm 0.04.$$

13.8 Long-baseline neutrino experiments

In recent years, intense accelerator-based neutrino beams, produced in a similar manner to that described in Section 12.2, have been used to study neutrino oscillations. One advantage of a neutrino beam experiment is that the energy spectrum can be tailored to a specific measurement. Long-baseline neutrino oscillation experiments typically use two detectors, one sufficiently close to the source of the beam to allow a measurement of the unoscillated neutrino energy spectrum, and one far from the source to measure the oscillated spectrum. The use of a near and far detector means that many systematic uncertainties cancel, allowing precise measurements to be made.

13.8.1 The MINOS experiment

The MINOS long-baseline neutrino oscillation experiment uses an intense 0.3 MW beam of muon neutrinos produced at Fermilab near Chicago. The neutrino energy spectrum is concentrated in the range 1–5 GeV and peaks at 3 GeV. The 1000 ton MINOS near detector is located 1 km from the source and the 5400 ton MINOS far detector is located in a mine in Northern Minnesota, 735 km from the source. The detectors are relatively simple, consisting of planes of iron, which provide the bulk of the mass, interleaved with planes of 4 cm wide strips of plastic scintillator. When a charged particle traverses the scintillator, light is produced. This scintillation light is transmitted to small PMTs using optical fibres that are embedded in the scintillator. The detector is magnetised to enable the measurement of the momentum of muons produced in $\nu_\mu N \to \mu^- X$ interactions from their curvature. The amount of scintillation light gives a measure of the energy of the hadronic final state X produced in the interaction. Hence, on an event-by-event basis, the neutrino energy is reconstructed, $E_\nu = E_\mu + E_X$. An example of a neutrino interaction in the MINOS detector is shown in Figure 13.21.

MINOS studied the neutrino oscillations of an almost pure ν_μ beam. Because θ_{13} is relatively small, $\nu_\mu \to \nu_\tau$ oscillations dominate. Since L is fixed, the oscillations are observed as a distortion of the energy spectrum. It is found that the first maximum of the oscillation probability occurs at 1.3 GeV. Despite the fact that the oscillations are dominated by $\nu_\mu \to \nu_\tau$, most of the oscillated ν_τ are below threshold for producing a tau-lepton and therefore MINOS makes a disappearance measurement of $|\Delta m^2_{32}|$ and θ_{32}. With the approximation $\Delta_{31} \approx \Delta_{32}$, the $\nu_\mu \to \nu_\mu$ survival probability is given by (13.34) with the U_{ei} replaced by $U_{\mu i}$,

$$P(\nu_\mu \to \nu_\mu) \approx 1 - 4|U_{\mu 1}|^2 U_{\mu 2}|^2 \sin^2 \Delta_{21} - 4|U_{\mu 3}|^2(1 - |U_{\mu 3}|^2) \sin^2 \Delta_{32}.$$

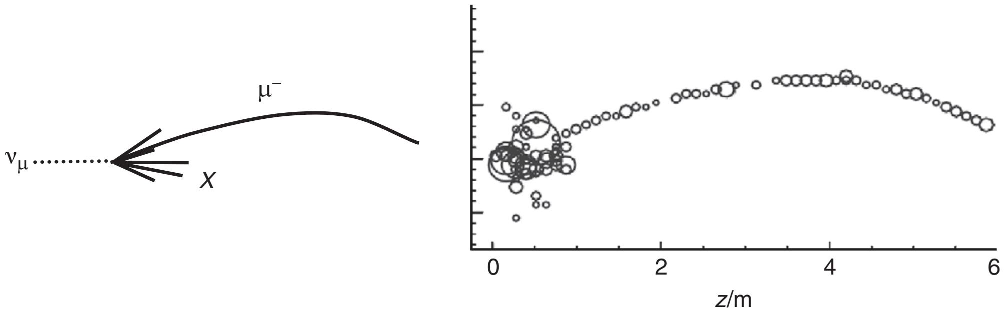

Fig. 13.21 A ν_μ charged-current weak interaction, $\nu_\mu N \to \mu^- X$, in the MINOS detector. The sizes of the circles indicate the amount of light recorded in the scintillator strips. The muon momentum is determined from the curvature in the magnetic field and the energy of the hadronic system from the amount of light close to the interaction vertex.

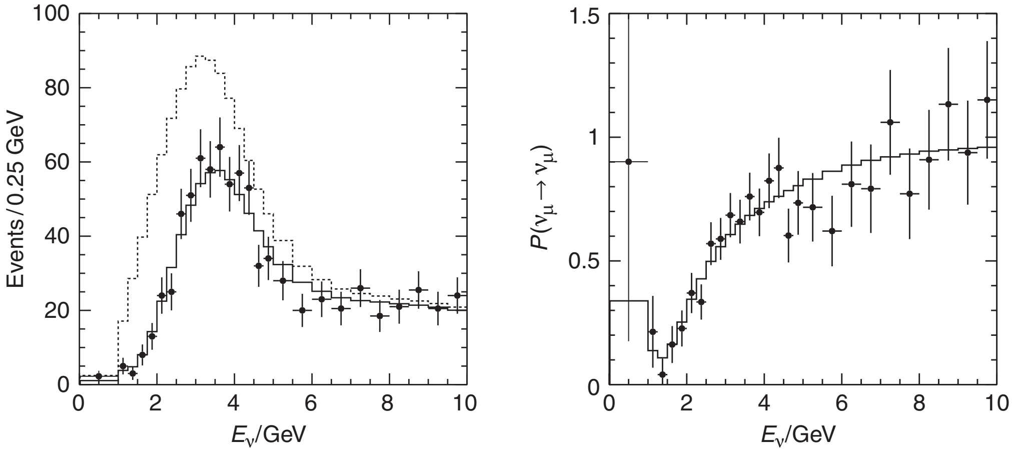

Fig. 13.22 Left: the MINOS far detector energy spectrum compared to the unoscillated prediction (dashed). Right: the oscillation probability as measured from the ratio of the far detector data to the unoscillated prediction. Adapted from Adamson *et al.* (2011).

For the MINOS experiment, with $L = 735\,\mathrm{km}$ and $E_\nu > 1\,\mathrm{GeV}$, the contribution to the oscillation probability from the long wavelength component associated with Δ_{21} can be neglected and therefore

$$P(\nu_\mu \to \nu_\mu) \approx 1 - 4|U_{\mu 3}|^2(1 - |U_{\mu 3}|^2)\sin^2\Delta_{32}.$$

Using the parameterisation of the PMNS matrix given in (13.33), this can be written

$$\begin{aligned} P(\nu_\mu \to \nu_\mu) &= 1 - 4\sin^2(\theta_{23})\cos^2(\theta_{13})\left[1 - \sin^2(\theta_{23})\cos^2(\theta_{13})\right]\sin^2\Delta_{32} \\ &= 1 - \left[\sin^2(2\theta_{23})\cos^4(\theta_{13}) + \sin^2(2\theta_{13})\sin^2(\theta_{23})\right]\sin^2\Delta_{32} \\ &\approx 1 - A\sin^2\left(\frac{\Delta m_{32}^2 L}{4E_\nu}\right), \end{aligned} \tag{13.38}$$

where $A = \sin^2(2\theta_{23})\cos^4(\theta_{13}) + \sin^2(2\theta_{13})\sin^2(\theta_{23})$. Because θ_{13} is relatively small the dominant term in the amplitude of the oscillations is from $\sin^2(2\theta_{23})\cos^4(\theta_{13})$.

By comparing the energy spectrum of charged-current neutrino interactions in the near and far detectors, MINOS directly measures the oscillation probability as a function of E_ν. Figure 13.22 shows the measured far detector energy spectrum compared to the expected spectrum for no oscillations, determined from the unoscillated near detector data. A clear deficit of neutrinos is observed at low energies, where the oscillation probability is highest. The right plot of Figure 13.22 shows the ratio of the measured far detector energy spectrum to the expectation without neutrino oscillations that is obtained from the near detector data. This provides a direct measurement of the survival probability $P(\nu_\mu \to \nu_\mu)$, albeit slightly smeared out by the experimental energy resolution. The position of the minimum in the measured oscillation curve at $E_\nu \sim 1.5\,\mathrm{GeV}$ determines

$$|\Delta m_{32}^2| = (2.3 \pm 0.1) \times 10^{-3}\,\mathrm{eV}^2.$$

The measured amplitude of the oscillations provides a measure of the parameter A, which, by using the known value of θ_{13}, provides a constraint on the mixing angle

$$\sin^2(2\theta_{23}) \gtrsim 0.90.$$

A slightly tighter constraint is obtained from the analysis of atmospheric neutrinos in the Super-Kamiokande detector.

13.9 The global picture

For reasons of space, it has only been possible to describe a few notable experiments that provide an illustration of the main experimental techniques used to study neutrino oscillations; there are other experiments. For example, the CERN to Gran Sasso neutrino experiment (CNGS) is searching for $\nu_\mu \to \nu_\tau$ appearance. At the time of writing, two candidate ν_τ interactions have been observed in the OPERA detector of the CNGS experiment. Furthermore, the T2K experiment in Japan is studying ν_μ disappearance and $\nu_\mu \to \nu_e$ appearance in an intense beam.

When the results from all experiments are taken together, a detailed picture of the properties of neutrinos emerges. The existence of neutrino oscillations implies that the neutrinos have mass, even if the masses are very small. The differences of the squares of the neutrino masses have been measured to better than 5% by the KamLAND and MINOS experiments,

$$\begin{aligned} m_2^2 - m_1^2 &= (7.6 \pm 0.2) \times 10^{-5}\,\mathrm{eV}^2, \\ |m_3^2 - m_2^2| &= (2.3 \pm 0.1) \times 10^{-3}\,\mathrm{eV}^2. \end{aligned}$$

Three of the four parameters of the PMNS matrix, describing the lepton flavour sector of the Standard Model, have been determined. From the recent results of the SNO, KamLAND, Super-Kamiokande, MINOS, Daya Bay, RENO and Double-Chooz experiments it is known that

$$\begin{aligned} &\sin^2(2\theta_{12}) = 0.87 \pm 0.04, \\ &\sin^2(2\theta_{23}) > 0.92, \\ &\sin^2(2\theta_{13}) \approx 0.10 \pm 0.01. \end{aligned}$$

From the above measurements, the magnitudes of the elements of PMNS matrix are determined to be approximately

$$\begin{pmatrix} |U_{e1}| & |U_{e2}| & |U_{e3}| \\ |U_{\mu1}| & |U_{\mu2}| & |U_{\mu3}| \\ |U_{\tau1}| & |U_{\tau2}| & |U_{\tau3}| \end{pmatrix} \sim \begin{pmatrix} 0.85 & 0.50 & 0.17 \\ 0.35 & 0.60 & 0.70 \\ 0.35 & 0.60 & 0.70 \end{pmatrix}. \tag{13.39}$$

The final parameter of the PMNS matrix, the phase δ, is not yet known. The focus of the next generation of experiments will be to measure this phase and thus establish whether CP is violated in leptonic weak interactions.

Summary

The ν_e, ν_μ and ν_τ are not fundamental particle states, but are mixtures of the mass eigenstates, ν_1, ν_2 and ν_3. The relationship between the weak and mass eigenstates is determined by the unitary PMNS matrix

$$\begin{pmatrix} \nu_e \\ \nu_\mu \\ \nu_\tau \end{pmatrix} = \begin{pmatrix} U_{e1} & U_{e2} & U_{e3} \\ U_{\mu1} & U_{\mu2} & U_{\mu3} \\ U_{\tau1} & U_{\tau2} & U_{\tau3} \end{pmatrix} \begin{pmatrix} \nu_1 \\ \nu_2 \\ \nu_3 \end{pmatrix}.$$

The PMNS matrix can be expressed in terms of four fundamental parameters of the Standard Model; three rotation angles, θ_{12}, θ_{13} and θ_{23}, and a complex phase δ that admits the possibility of CP violation in the leptonic sector.

Neutrinos propagate as coherent linear superpositions of the mass eigenstates, for example

$$|\nu_e\rangle = U_{e1}|\nu_1\rangle e^{-i\phi_1} + U_{e2}|\nu_2\rangle e^{-i\phi_2} + U_{e3}|\nu_3\rangle e^{-i\phi_3}.$$

If $m(\nu_1) \neq m(\nu_2) \neq m(\nu_3)$, phase differences develop between the different components, giving rise to the observable effect of neutrino oscillations, with oscillation probabilities of the form

$$P(\nu_e \to \nu_\mu) = \sin^2(2\theta)\sin^2\left(1.27\frac{\Delta m^2[\mathrm{eV}^2]L[\mathrm{km}]}{E_\nu[\mathrm{GeV}]}\right).$$

The study of neutrino oscillations provides a determination of the differences in the squares of the neutrino masses

$$m_2^2 - m_1^2 \approx 7.6\times10^{-5}\,\mathrm{eV}^2 \quad \text{and} \quad |m_3^2 - m_2^2| \approx 2.3\times10^{-3}\,\mathrm{eV}^2,$$

and measurements of the mixing angles of the PMNS matrix

$$\theta_{12} \approx 35^\circ,\ \ \theta_{23} \approx 45^\circ \ \text{ and } \ \theta_{13} \approx 10^\circ.$$

Problems

13.1 By writing $p_1 = \beta E_1$ and $p_2 = \beta E_2$, and assuming $\beta_1 = \beta_2 = \beta$, show that Equation (13.13) reduces to (13.12), i.e.

$$\Delta\phi_{12} = (E_1 - E_2)\left[T - \left(\frac{E_1 + E_2}{p_1 + p_1}\right)L\right] + \left(\frac{m_1^2 - m_2^2}{p_1 + p_2}\right)L \approx \frac{m_1^2 - m_2^2}{2p}L,$$

where $p = p_1 \approx p_2$ and it is assumed that $p_1 \gg m_1$ and $p_2 \gg m_2$.

13.2 Show that when L is given in km and Δm^2 is given in eV^2, the two-flavour oscillation probability expressed in natural units becomes

$$\sin^2(2\theta)\sin^2\left(\frac{\Delta m^2[\mathrm{GeV}^2]L[\mathrm{GeV}^{-1}]}{4E_\nu[\mathrm{GeV}]}\right) \rightarrow \sin^2(2\theta)\sin^2\left(1.27\frac{\Delta m^2[\mathrm{eV}^2]L[\mathrm{km}]}{4E_\nu[\mathrm{GeV}]}\right).$$

13.3 From Equation (13.24) and the unitarity relation of (13.18), show that

$$\begin{aligned}P(\nu_e \rightarrow \nu_e) = 1 &+ 2|U_{e1}|^2|U_{e2}|^2\,\Re e\{[e^{-i(\phi_1-\phi_2)} - 1]\}\\ &+ 2|U_{e1}|^2|U_{e3}|^2\,\Re e\{[e^{-i(\phi_1-\phi_3)} - 1]\}\\ &+ 2|U_{e2}|^2|U_{e3}|^2\,\Re e\{[e^{-i(\phi_2-\phi_3)} - 1]\}.\end{aligned}$$

13.4 Derive Equation (13.30) in the following three steps.

(a) By writing the oscillation probability $P(\nu_e \rightarrow \nu_\mu)$ as

$$P(\nu_e \rightarrow \nu_\mu) = 2\sum_{i<j}\Re e\left\{U_{ei}^*U_{\mu i}U_{ej}U_{\mu j}^*\left[e^{i(\phi_j-\phi_i)} - 1\right]\right\},$$

and writing $\Delta_{ij} = (\phi_i - \phi_j)/2$, show that

$$\begin{aligned}P(\nu_e \rightarrow \nu_\mu) = &-4\sum_{i<j}\Re e\{U_{ei}^*U_{\mu i}U_{ej}U_{\mu j}^*\}\sin^2\Delta_{ij}\\ &+2\sum_{i<j}\Im m\{U_{ei}^*U_{\mu i}U_{ej}U_{\mu j}^*\}\sin 2\Delta_{ij}.\end{aligned}$$

(b) Defining $-J \equiv \Im m\{U_{e1}^*U_{\mu 1}U_{e3}U_{\mu 3}^*\}$, use the unitarity of the PMNS matrix to show that

$$\Im m\{U_{e1}^*U_{\mu 1}U_{e3}U_{\mu 3}^*\} = -\Im m\{U_{e2}^*U_{\mu 2}U_{e3}U_{\mu 3}^*\} = -\Im m\{U_{e1}^*U_{\mu 1}U_{e2}U_{\mu 2}^*\} = -J.$$

(c) Hence, using the identity

$$\sin A + \sin B - \sin(A+B) = 4\sin\left(\frac{A}{2}\right)\sin\left(\frac{B}{2}\right)\sin\left(\frac{A+B}{2}\right),$$

show that

$$P(\nu_e \rightarrow \nu_\mu) = -4\sum_{i<j}\Re e\{U_{ei}^*U_{\mu i}U_{ej}U_{\mu j}^*\}\sin^2\Delta_{ij} + 8J\sin\Delta_{12}\sin\Delta_{13}\sin\Delta_{23}.$$

(d) Hence show that

$$P(\nu_e \rightarrow \nu_\mu) - P(\overline{\nu}_e \rightarrow \overline{\nu}_\mu) = 16\,\Im m\{U_{e1}^*U_{\mu 1}U_{e2}U_{\mu 2}^*\}\sin\Delta_{12}\sin\Delta_{13}\sin\Delta_{23}.$$

(e) Finally, using the current knowledge of the PMNS matrix determine the maximum possible value of $P(\nu_e \rightarrow \nu_\mu) - P(\overline{\nu}_e \rightarrow \overline{\nu}_\mu)$.

13.5 The general unitary transformation between mass and weak eigenstates for two flavours can be written as

$$\begin{pmatrix} \nu_e \\ \nu_\mu \end{pmatrix} = \begin{pmatrix} \cos\theta \exp(i\delta_1) & \sin\theta \exp\left(i\left[\frac{\delta_1+\delta_2}{2} - \delta\right]\right) \\ -\sin\theta \exp\left(i\left[\frac{\delta_1+\delta_2}{2} + \delta\right]\right) & \cos\theta \exp(i\delta_2) \end{pmatrix} \begin{pmatrix} \nu_1 \\ \nu_2 \end{pmatrix}.$$

(a) Show that the matrix in the above expression is indeed unitary.

(b) Show that the three complex phases δ_1, δ_2 and δ can be eliminated from the above expression by the transformation

$$\ell_\alpha \rightarrow \ell_\alpha e^{i(\theta_e+\theta'_\alpha)}, \quad \nu_k \rightarrow \nu_k e^{i(\theta_e+\theta'_k)} \quad \text{and} \quad U_{\alpha k} \rightarrow U_{\alpha k} e^{i(\theta'_\alpha-\theta'_k)},$$

without changing the physical form of the two-flavour weak charged current

$$-i\frac{g_W}{\sqrt{2}}\,(\overline{e},\, \overline{\mu})\,\gamma^\mu \tfrac{1}{2}(1-\gamma^5) \begin{pmatrix} U_{e1} & U_{e2} \\ U_{\mu 1} & U_{\mu 2} \end{pmatrix} \begin{pmatrix} \nu_1 \\ \nu_2 \end{pmatrix}.$$

13.6 The derivations of (13.37) and (13.38) used the trigonometric relations

$$1 - \tfrac{1}{2}\sin^2(2\theta_{13}) = \cos^4(\theta_{13}) + \sin^4(\theta_{13}),$$

and

$$4\sin^2\theta_{23}\cos^2\theta_{13}(1-\sin^2\theta_{23}\cos^2\theta_{13}) = (\sin^2 2\theta_{23}\cos^4\theta_{13} + \sin^2 2\theta_{13}\sin^2\theta_{23}).$$

Convince yourself these relations hold.

13.7 Use the data of Figure 13.20 to obtain estimates of $\sin^2(2\theta_{12})$ and $|\Delta m^2_{21}|$.

13.8 Use the data of Figure 13.22 to obtain estimates of $\sin^2(2\theta_{23})$ and $|\Delta m^2_{32}|$.

13.9 The T2K experiment uses an off-axis ν_μ beam produced from $\pi^+ \rightarrow \mu^+\nu_\mu$ decays. Consider the case where the pion has velocity β along the z-direction in the laboratory frame and a neutrino with energy E^* is produced at an angle θ^* with respect to the z'-axis in the π^+ rest frame.

(a) Show that the neutrino energy in the pion rest frame is $p^* = (m^2_\pi - m^2_\mu)/2m_\pi$.

(b) Using a Lorentz transformation, show that the energy E and angle of production θ of the neutrino in the laboratory frame are

$$E = \gamma E^*(1+\beta\cos\theta^*) \quad \text{and} \quad E\cos\theta = \gamma E^*(\cos\theta^* + \beta),$$

where $\gamma = E_\pi/m_\pi$.

(c) Using the expressions for E^* and θ^* in terms of E and θ, show that

$$\gamma^2(1-\beta\cos\theta)(1+\beta\cos\theta^*) = 1.$$

(d) Show that maximum value of θ in the laboratory frame is $\theta_{\max} = 1/\gamma$.

(e) In the limit $\theta \ll 1$, show that

$$E \approx 0.43 E_\pi \frac{1}{1+\beta\gamma^2\theta^2},$$

and therefore on-axis ($\theta = 0$) the neutrino energy spectrum follows that of the pions.

(f) Assuming that the pions have a flat energy spectrum in the range 1–5 GeV, sketch the form of the resulting neutrino energy spectrum at the T2K far detector (Super-Kamiokande), which is off-axis at $\theta = 2.5°$. Given that the Super-Kamiokande detector is 295 km from the beam, explain why this angle was chosen.